

Coherent phase locking, collective oscillations, and stability in coupled vertical-cavity-surface emitting laser arrays

S. Riyopoulos

Science Applications International Corporation, McLean, Virginia 22102

(Received 17 June 2002; published 26 November 2002)

Closely packed vertical-cavity-surface emitting laser arrays support collective modes via nearest-neighbor interactions. Nonlinear cavity-lattice dynamic equations are introduced through the derivation of intercavity coupling coefficients based on microscopic transition probabilities and the tight-binding approximation for lattice eigenstates. Ultrafast numerical simulations show array relaxation to phase-locked steady-state configurations, of fixed phase difference among nearest neighbors. Linear stability analysis derives the dispersion relation of the collective modes excited over the cavity lattice, their stability regimes, and transitions to limit cycles and chaotic behavior at high coupling strengths. Spontaneous phase selection is also analyzed.

DOI: 10.1103/PhysRevA.66.053820

PACS number(s): 42.55.Px, 42.60.Fc, 42.60.Da

I. INTRODUCTION

Vertical-cavity-surface emitting laser (VCSEL) arrays [1] are recently finding a variety of applications ranging from interconnects and optical switch fabrics to phased arrays and beam steering. As the packing density increases, lateral interactions among cavities become important and influence system performance. Induced cross-channel talk and BER is a subject of concern for optical interconnects. On the other hand spontaneous phase locking offers the opportunity for phased array operation for coherent high power generation and beam steering applications. Phase-locked VCSEL array operation has been experimentally observed [2–4]. The steady-state eigenmode structure, involving the passive (real diffraction index) coupling among either guided cavity eigenmodes through their evanescent fields [5], or antiguided modes through laterally “leaking” radiation [6], has been analyzed. However little attention has been paid to the dynamic array aspects, such as the transition to steady state, stability of the phase locking, and the possibility of dynamic control of the locked phase. In addition, *active* coupling stemming from the mutually induced polarization among adjacent cavities and amounting to the complex gain contribution to the diffraction index has been neglected. A dynamic system approach introducing the actively coupled intercavity rate equations is employed here to address the above issues.

Periodic arrangements of VCSEL microcavities separated by distances comparable to the $1/e^2$ transverse length of the cavity mode intensity interact with their fringe fields. Such interactions, caused by induced cross polarization during stimulated transitions, include cross gain and cross-hole burning among nearest-neighbor cavities. Since each VCSEL possesses a cavity oscillation frequency [7] the cavity array constitutes a coupled oscillator lattice admitting collective oscillation modes. A systematic analytic derivation of the cross-coupling terms and the resulting coupled rate equations describing the dynamics of one-dimensional (1D) or 2D periodic arrays of identical cavities is performed. Our numerical simulations and analytic investigation of the derived “lattice dynamics” equations demonstrate the following.

(1) Under constant drive current and for random initial

conditions the arrays settle to the phase-locked steady state, with the same fixed phase difference $\Delta\varphi$ between any two neighbors.

(2) Perturbations about the steady-state propagate as collective oscillations (Bloch-type modulation waves) over the array, and are characterized by a given dispersion relation.

(3) For high values of the coupling constant, instead of steady state we have limit cycle oscillations and finally chaotic array behavior under applied cavity biases constant in time and uniform in space.

The first conclusion implies that VCSEL arrays are *inherently phase locked*, provided the mutual interaction strength is not too strong but exceeds some environmental randomization floor. For L_x , L_y -periodic boundary conditions the phase shift among adjacent cavities settles at $\Delta\varphi = \mathbf{K} \cdot \mathbf{b}$, where \mathbf{b} is the lattice period and \mathbf{K} may assume any of the discrete values $n(2\pi/L_x)\hat{\mathbf{x}} + m(2\pi/L_y)\hat{\mathbf{y}}$. In effect we have a “crystallization” of the individual cavity modes into a standing Bloch wave. The second conclusion predicts the excitation of stable photonic “vibrations” over a phase-locked lattice. Since we deal with low-frequency coherent variations of the electron-photon densities we may designate these modes as photonic sound. Finally, a steady state is dissolved at high coupling strengths, i.e., at very close array packing. This is consistent with the generic behavior of nonlinear dissipative systems which develop spatiotemporal patterns under an external driving bias uniform in space and constant in time.

We clarify that the above phase-locking interactions and the related low-frequency (gigahertz range) modulation waves result from *active* cavity coupling, distinctively different from the passive interference due to periodic index variation responsible for the photonic band-gap dispersion [8]. Instead of multicavity photon interference due to coherent diffraction, the examined phenomenon results from coherent cross-cavity photon absorption and reemission. Active coupling among laterally confined modes applies to guided cavity modes as well as band-gap modes in active photonic defects [9], and occurs through the overlapping of the evanescent lateral fields, without fast wave propagation in

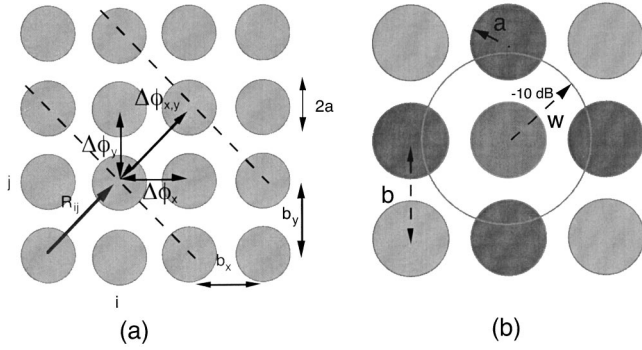


FIG. 1. (a) Schematic 2D array configuration. When phase locked, the same phase difference applies between any two neighbors in the x and in the y direction (in general, $\Delta\varphi_x \neq \Delta\varphi_y$). (b) Schematic cross-gain and cross-hole burning interactions among near neighbors.

the lateral (transverse) direction.¹ An analogy can be drawn from solid-state physics, whereby photonic modes are similar to “free” electron (propagating) wave functions coupled through the lattice periodicity, while the present cavity lattice modes are similar to the tight-binding wave functions resulting from the near-neighbor coupling of confined orbitals. In addition, in this approach, the steady-state modal parameters, such as peak amplitude and average density at each site, emerge from the zeros of the dynamic equations, rather than from steady-state perturbation theory.

Cross-current leakage among neighboring cavities as well as long-range thermal coupling are neglected, since the characteristic times for carrier and heat diffusion are much longer than the optical coupling time and the $1/\Omega$ period.

An earlier lattice model [10] neglected the steady-state phase coupling, assuming that all phase-dependent interactions come during the perturbations about a zero-phase-shifted $\Delta\varphi_o = 0$ lattice equilibrium. The earlier obtained dispersion for lattice oscillations corresponds to the $\Delta\varphi_o = 0$ limit of the general dispersion relation Eq. (44) here. However, only the *ab initio* introduction of the phase coupling in this paper allows for the spontaneous phase locking at steady state.

II. RATE EQUATIONS FOR COUPLED VCSEL CAVITIES

In Fig. 1 we assume that MN identical cavities are arranged in the x - y plane with axes along the z direction and thin circular active areas centered at the lattice vectors $\mathbf{R}_{ij} = i\mathbf{b}_x + j\mathbf{b}_y$, with \mathbf{b}_x , \mathbf{b}_y being the x and y period (basis vectors). Hence, we are dealing with radiation propagation in a medium of uniform dielectric constant ϵ , caused by the bound carrier response, and a superimposed periodic complex gain distribution reflecting the periodic electron-hole pair density \mathcal{N} in the active regions,

¹Paraxial cavity eigenmodes, such as the GL modes, involve a small nonevanescing transverse $k_\perp/k_z \ll 1$, however their Gaussian decay in the transverse direction qualifies as fringe field interaction.

$$\mathcal{N}(\mathbf{r}) = \sum_{i,j} N_{ij}(t) \chi(\mathbf{r} - \mathbf{R}_{ij}), \quad (1)$$

where N_{ij} is the cross-section averaged density and $\chi(\mathbf{r})$ its normalized profile. Without loss of generality a cylindrically uniform step-function profile, $\chi(\mathbf{r}) = 1$, $r \leq a$ and zero otherwise, is chosen so that $(1/\pi a^2) \int d\mathbf{r}^2 \chi(\mathbf{r}) = 1$. For weakly coupled cavities, characterized by laterally confined modes interacting through their fringe fields, the radiation field is expressed as a linear superposition of isolated cavity modes. Since the paraxial approximation $k_\perp/k_z \ll 1$ holds for the guided cavity modes (or for gap modes in active photonic defects) the total radiation is given by a paraxial mode superposition of slowly varying complex amplitudes $\mathcal{E}_{ij}(t)$ and eigenmode envelopes $U^{mp}(\bar{\mathbf{r}})$ centered around lattice vectors $\bar{\mathbf{r}} = \mathbf{r} - \mathbf{R}_{ij}$,

$$\mathbf{E} = \sum_{i,j} \mathcal{E}_{ij}^{mp}(t) \sum_{m,p} U^{mp}(\mathbf{r} - \mathbf{R}_{ij}) e^{i\psi_{mn}(z)} e^{i(kz - \omega_{mp}t)}. \quad (2)$$

In addition to the usual orthonormality among same cavity paraxial modes, $\int d^2\mathbf{r} U^{mp*}(\mathbf{r}) U^{nq}(\mathbf{r}) = \delta_{mn} \delta_{pq}$, spatial orthonormality holds among same modal profiles m, p around different lattice sites (Appendix A),

$$\begin{aligned} \int d^2\mathbf{r} U^*(\mathbf{r} - \mathbf{R}_{ij}) U(\mathbf{r} - \mathbf{R}_{i'j'}) &= \delta_{i,i'} \delta_{j,j'}, \\ \int d^2\mathbf{r} \chi^*(\mathbf{r} - \mathbf{R}_{ij}) \chi(\mathbf{r} - \mathbf{R}_{i'j'}) &= \delta_{i,i'} \delta_{j,j'}. \end{aligned} \quad (3)$$

We assumed the same electric-field polarization $\hat{\mathbf{e}}$ for all cavities, aligned with $\hat{\mathbf{x}}$. The uniform medium dispersion is $\omega_{mp} = k_{mp}c/\sqrt{\epsilon}$, where k_{mp} is defined by the cavity resonance $k_{mp} = (2\pi + \psi_{mp})/L$, including the correction $\psi_{mp} = (1 + 2m + p)L/2b$ from the slow phase paraxial envelope $\psi_{mp}(L) \equiv L(k - k_z)$. The sought after photonic modulation frequency is near the natural cavity oscillation frequency, $(d/dt) \ln \mathcal{E} \approx \Omega$, usually much smaller than the frequency separation among cavity modes $\omega_{mp} - \omega_{m'p'}$. Thus one can ignore resonant coupling between cross-modal beating $\Delta\omega_{mp}$ and lattice oscillations, and pick a single mode mp ; without loss of generality we choose the fundamental $m=0, p=0$, and $U \equiv U_\infty$.

Substituting Eq. (2) in the paraxial wave equation and keeping lowest-order terms in the time derivative $d\mathcal{E}/dt$ yields

$$\begin{aligned} \mathcal{E}_{ij} U(\mathbf{r} - \mathbf{R}_{ij}) e^{i\psi(z)} &\left(-k^2 + \frac{\omega^2}{c^2} \epsilon \right) \\ &+ \mathcal{E}_{ij} \left(\nabla_\perp^2 + 2ik \frac{\partial}{\partial z} \right) U(\mathbf{r} - \mathbf{R}_{ij}) e^{i\psi(z)} \\ &+ U(\mathbf{r} - \mathbf{R}_{ij}) e^{i\psi(z)} \frac{2i\omega}{c^2} \epsilon \frac{\partial \mathcal{E}_{ij}}{\partial t} \\ &= \frac{4\pi\omega^2}{c^2} \mathcal{P}_{ij}. \end{aligned} \quad (4)$$

Use of the zeroth-order dispersion in the first line and the defining relation for the paraxial eigenmodes $U(\mathbf{r})e^{i\psi(z)}$ in the second leaves the slow envelope equation

$$\sum_{ij} U(\mathbf{r}-\mathbf{R}_{ij})e^{i\psi(z)}\frac{\partial\mathcal{E}_{ij}}{\partial t} = -\frac{4\pi i}{2\epsilon}\omega\mathcal{P}_{ij}(\mathbf{r}). \quad (5)$$

The polarization \mathcal{P} on the right-hand side reflects the induced electron-hole dipole moment during stimulated emission. It is given by

$$\mathcal{P} = p\rho_{eh} = p\frac{\mathbf{p}\cdot\mathbf{E}}{i\hbar}\frac{1}{-i\Delta\omega-\Gamma}\mathcal{N}, \quad (6)$$

where $\mathbf{p} = \langle e|\mathbf{e}r|h\rangle$ is the microscopic transition dipole moment between the electron $\langle e|$ and hole $|h\rangle$ states, $p = \mathbf{p}\cdot\hat{\mathbf{e}}$ and \mathcal{N} represents the population inversion, i.e., the overequilibrium excess of the electron-hole pair density. Substitution of Eqs. (1) and (2) on the right-hand side (rhs) of Eq. (6) casts Eq. (5) as

$$\begin{aligned} & \sum_{ij} U(\mathbf{r}-\mathbf{R}_{ij})e^{i\psi(z)}\frac{\partial\mathcal{E}_{ij}}{\partial t} \\ &= \frac{2\pi\omega}{\hbar\epsilon}\frac{p^2}{i\Delta\omega+\Gamma}\sum_{ij}\mathcal{N}_{ij}(t)\mathcal{E}_{ij}(t)\chi(\mathbf{r}-\mathbf{R}_{ij}) \\ & \quad \times U(\mathbf{r}-\mathbf{R}_{ij})e^{i\psi(z)}. \end{aligned} \quad (7)$$

The evolution for the population inversion $\mathcal{N} = \rho_{ee} - \rho_{hh}$ is given by

$$\frac{\partial\mathcal{N}}{\partial t} = \frac{J}{ed_w} - \gamma\mathcal{N} - \left(\frac{p}{\hbar}\right)^2\mathbf{E}\cdot\mathbf{E}^*\frac{\Gamma}{\Delta\omega^2+\Gamma^2}\mathcal{N}, \quad (8)$$

whereby the use of Eqs. (1) and (2) and the definition of the pump strength $\Lambda_{ij} \equiv J_{ij}/ed_w$ yields

$$\begin{aligned} \sum_{ij}\chi(\mathbf{r}-\mathbf{R}_{ij})\frac{\partial\mathcal{N}_{ij}}{\partial t} &= \sum_{ij}\chi(\mathbf{r}-\mathbf{R}_{ij})\Lambda_{ij} - \gamma\sum_{ij}\chi(\mathbf{r}-\mathbf{R}_{ij})\mathcal{N}_{ij} - \left(\frac{p}{\hbar}\right)^2\frac{\Gamma}{\Delta\omega^2+\Gamma^2}\sum_{ij}\mathcal{N}_{ij}(t)\chi(\mathbf{r}-\mathbf{R}_{ij}) \\ & \quad \times \left\{ \sum_{i'j'}\mathcal{E}_{ij}(t)\mathcal{E}_{i'j'}^*(t)U(\mathbf{r}-\mathbf{R}_{ij})U^*(\mathbf{r}-\mathbf{R}_{i'j'}) + \text{c.c.} \right\}. \end{aligned} \quad (9)$$

Equations (7) and (9) describe spatially distributed interactions over the cavity lattice. They are reduced to equations for the field amplitude and the average density evolution at the ij th cavity by a projection onto the local profiles. The complex electric-field amplitude evolution is obtained from the integral projection onto the $U(\mathbf{r}-\mathbf{R}_{ij})$ wave function, taking advantage of the orthonormality (3), and yielding

$$\frac{\partial\mathcal{E}_{ij}}{\partial t} = \frac{2\pi p^2}{\hbar}\frac{\omega(\Gamma-i\Delta\omega)}{\Delta\omega^2+\Gamma^2}\left[\mathcal{N}_{ij}\mathcal{E}_{ij} + \sum_{i'\neq i, j'\neq j}\Lambda_{ij;i'j'}\mathcal{N}_{i'j'}\mathcal{E}_{ij} + Y_{ij;i'j'}(\mathcal{N}_{ij}\mathcal{E}_{i'j'} + \mathcal{N}_{i'j'}\mathcal{E}_{ij})\right]. \quad (10)$$

In a similar manner, the integral projection of the global carrier density (9) with $\chi(\mathbf{r}-\mathbf{R}_{ij})$ yields the carrier evolution in the ij th cavity,

$$\frac{\partial\mathcal{N}_{ij}}{\partial t} = \frac{J_{ij}}{ed_w} - \gamma\mathcal{N}_{ij} - \left(\frac{p}{\hbar}\right)^2\frac{\Gamma}{\Delta\omega^2+\Gamma^2}\left[\mathcal{N}_{ij}\mathcal{E}_{ij}\mathcal{E}_{ij}^* + \sum_{i'\neq i, j'\neq j}\Lambda_{ij;i'j'}\mathcal{N}_{ij}\mathcal{E}_{i'j'}\mathcal{E}_{i'j'}^* + \sum_{i'\neq i, j'\neq j}(Y_{ij;i'j'}\mathcal{N}_{ij}\mathcal{E}_{i'j'}\mathcal{E}_{ij}^* + \text{c.c.})\right], \quad (11)$$

where the step-function property $\chi^2(\mathbf{r}) = \chi(\mathbf{r})$ for the uniform carrier density profile in each cavity was used. Above, $\zeta = (d_w/L)\int_0^\infty d^2\mathbf{r}U^*(\mathbf{r})\chi(\mathbf{r})U(\mathbf{r})$ is the *gain confinement factor*, d_w being the quantum well thickness and L the mirror separation. The intercavity coupling strengths are given by the following terms:

$$\begin{aligned}
\Lambda_{i'-i,j'-j} &= \int_0^\infty d^2\mathbf{r} U^*(\mathbf{r}-\mathbf{R}_{ij}) \chi(\mathbf{r}-\mathbf{R}_{i'j'}) U(\mathbf{r}-\mathbf{R}_{ij}) \\
&= \int_0^\infty d^2\mathbf{r} U^*(\mathbf{r}) \chi(\mathbf{r}-\Delta\mathbf{R}_{i-i',j-j'}) U(\mathbf{r}) \\
&= \int_0^\infty d^2\mathbf{r} U^*(\mathbf{r}+\Delta\mathbf{R}_{i-i',j-j'}) \chi(\mathbf{r}) \\
&\quad \times U(\mathbf{r}+\Delta\mathbf{R}_{i-i',j-j'}), \tag{12}
\end{aligned}$$

$$\begin{aligned}
Y_{i'-i,j'-j} &= \int_0^\infty d^2\mathbf{r} U^*(\mathbf{r}-\mathbf{R}_{ij}) \chi(\mathbf{r}-\mathbf{R}_{ij}) U(\mathbf{r}-\mathbf{R}_{i'j'}) \\
&= \int_0^\infty d^2\mathbf{r} U^*(\mathbf{r}) \chi(\mathbf{r}) U(\mathbf{r}-\Delta\mathbf{R}_{i-i',j-j'}) \\
&= \int_0^\infty d^2\mathbf{r} U^*(\mathbf{r}+\Delta\mathbf{R}_{i-i',j-j'}) \\
&\quad \times \chi(\mathbf{r}+\Delta\mathbf{R}_{i-i',j-j'}) U(\mathbf{r}). \tag{13}
\end{aligned}$$

Due to the periodicity the coupling coefficients depend only on the separation distance $\Delta\mathbf{R}_{i-i',j-j'} = \mathbf{R}_{ij} - \mathbf{R}_{i'j'}$ among lattice sites, implying $\Lambda_{ij;i'j'} \equiv \Lambda_{i'-i,j'-j}$, $Y_{ij;i'j'} \equiv Y_{i'-i,j'-j}$. The Hermitian property is also satisfied, taking the form $\Lambda_{i-i',j-j'}^* = \Lambda_{i'-i,j'-j}$, etc. We pause to note that the use of radially truncated carrier densities without overlapping diffusion tails, evident in the asymmetry

$$\int_0^\infty d^2\mathbf{r} U(\mathbf{r}) f(\mathbf{r}) U(\mathbf{r}-\Delta\mathbf{R}_{i-i',j-j'}) \neq 0, \tag{14}$$

$$\int_0^\infty d^2\mathbf{r} \chi(\mathbf{r}) f(\mathbf{r}) \chi(\mathbf{r}-\Delta\mathbf{R}_{i-i',j-j'}) = 0 \tag{15}$$

for arbitrary $f(\mathbf{r}) \neq 1$, means neglecting cavity interaction by carrier leakage. Intercavity coupling is dominated by radiation overlap, a valid approximation, given the disparity between the radiative and the much slower diffusion time scales.²

III. NEAREST-NEIGHBOR COUPLED ARRAY MODEL

The evolution of the complex $\mathcal{E}_{ij} \equiv E_{ij} \exp(i\varphi_{ij})$ is finally separated into amplitude and phase evolution according to

$$\frac{dE_{ij}}{dt} = \frac{1}{2E_{ij}} \left(\mathcal{E}_{ij}^* \frac{\partial \mathcal{E}_{ij}}{\partial t} + \text{c.c.} \right), \tag{16}$$

²A most general treatment including carrier leakage with diffuse density profiles $\chi'(\mathbf{r}) \neq \chi(\mathbf{r})$ adds nonzero current coupling terms from Eq. (15) in the carrier balance equation (12); also $\chi'^2(\mathbf{r}) \neq \chi^2(\mathbf{r})$ causes modified Λ' and Y' terms in the carrier balance equation (12), breaking the coupling coefficient symmetry between carrier and radiation rate equations.

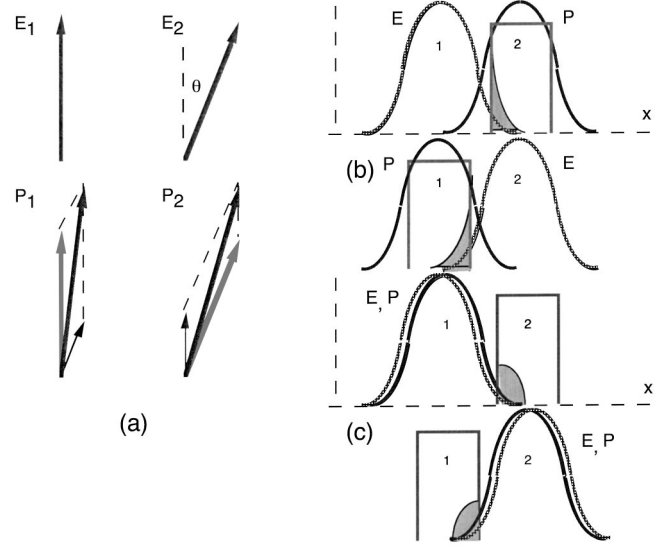


FIG. 2. Schematic illustration of intercavity interactions. (a) Polar representation of the unperturbed electric-field vectors (up) and the mutually induced polarizations (down). (b) Cross polarization 1 \rightarrow 2 effect. Spatial profile of the electric field in cavity 1 and the self-polarization in cavity 2. Also shown, the square density profile for cavity 2 and the shaded area of the E_1P_2 integral. Mirror image interaction 2 \rightarrow 1 shown below (b). Up: cross gain, where the electric field of cavity 1 overlaps with its own induced polarization in cavity 2. Its mirror image below is also interpreted as cross-hole burning induced by cavity 2 into cavity 1.

$$\frac{d\varphi_{ij}}{dt} = \frac{1}{2iE_{ij}^2} \left(\mathcal{E}_{ij}^* \frac{\partial \mathcal{E}_{ij}}{\partial t} - \text{c.c.} \right). \tag{17}$$

Substituting Eqs. (10)–(12) into the rhs of Eqs. (16) and (17) yields

$$\begin{aligned}
\frac{dE_{ij}}{dt} &= \text{Re} \left\{ \mathcal{G}(\omega) \left[\mathcal{N}_{ij} E_{ij} + \sum_{i' \neq i, j' \neq j} \{ \Lambda_{ij;i'j'} \mathcal{N}_{i'j'} E_{ij} \right. \right. \\
&\quad \left. \left. + Y_{ij;i'j'} (\mathcal{N}_{ij} E_{i'j'} + \mathcal{N}_{i'j'} E_{ij}) e^{i(\varphi_{i'j'} - \varphi_{ij})} \right] \right\}, \tag{18}
\end{aligned}$$

$$\begin{aligned}
\frac{d\varphi_{ij}}{dt} &= \text{Im} \left\{ \mathcal{G}(\omega) \left[\mathcal{N}_{ij} + \sum_{i' \neq i, j' \neq j} \left\{ \Lambda_{ij;i'j'} \mathcal{N}_{i'j'} \right. \right. \right. \\
&\quad \left. \left. + Y_{ij;i'j'} \left(\mathcal{N}_{ij} \frac{E_{i'j'}}{E_{ij}} + \mathcal{N}_{i'j'} \frac{E_{ij}}{E_{i'j'}} \right) e^{i(\varphi_{i'j'} - \varphi_{ij})} \right] \right\}, \tag{19}
\end{aligned}$$

where

$$\mathcal{G}(\omega) \equiv \frac{2\pi p^2}{\hbar} \frac{\omega(\Gamma - i\Delta\omega)}{\Delta\omega^2 + \Gamma^2}. \tag{20}$$

The distinctive physical origin of $\Lambda_{ij;i'j'}$ and $Y_{ij;i'j'}$ becomes transparent from the above equations, as illustrated in Fig. 2. The total induced polarization in each cavity is the

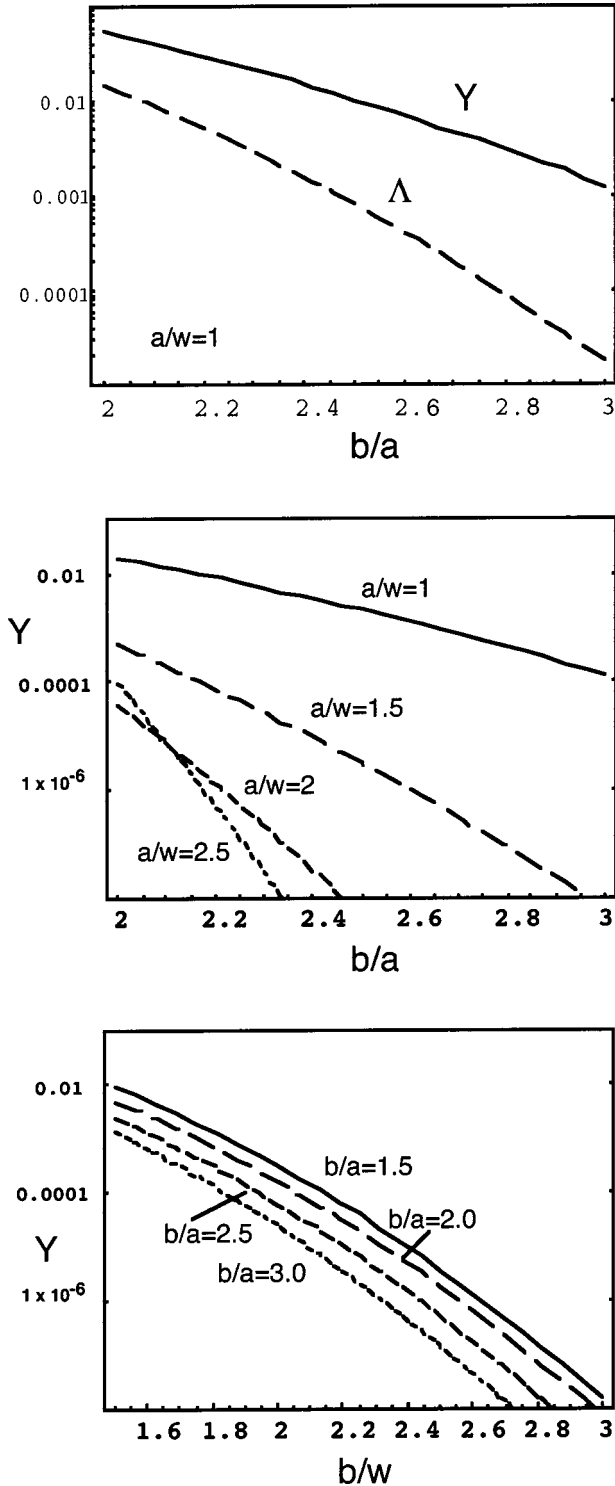


FIG. 3. Dependence of coupling coefficient strength on lattice geometry. (a) Λ and Y vs cavity separation b/a for the fixed cavity radius-to-mode waist $a/w=1$. (b) Y vs separation b/a for various relative waist sizes a/w . (c) Y vs b/w at various cavity separations b/a .

vector sum of the response to its own electric field plus its adjacent cavity phase-shifted fields, Fig. 3. The cross polarization $Y_{ij;i'j'}$ terms involve the coupling of the self-induced polarization in one site to the fields of its neighbor sites, Fig.

2(b), and introduce the phase dependence. The cross-gain terms $\Lambda_{ij;i'j'}$ mitigate interactions where the polarization induced by one site to its neighbors couples back into the gain of the original site, Fig. 2(c), and is phase independent.

Defining the photon flux density $F \equiv P/\hbar\omega$ and the photon density $N_p = F/v_g$, where $P = v_k \epsilon E E^*/8\pi$ is the Poynting vector and v_k is the group velocity, it follows by multiplying both sides of Eq. (18) by $v_k \epsilon E_{ij}/4\pi\hbar\omega$ that both the photon and carrier rates dN/dt , dN_p/dt are proportional to the stimulated emission rate

$$\mathcal{R} = \left(\frac{pE}{\hbar} \right)^2 \frac{\Gamma}{\Delta\omega^2 + \Gamma^2}. \quad (21)$$

The density \mathcal{N}_{ij} in fact represents the carrier density of states over a resonant interval $\Delta\epsilon = \hbar\Gamma$ around the transition energy $\epsilon_o = \hbar\omega$,

$$\mathcal{R}\mathcal{N}_{ij} \rightarrow \frac{1}{V_c} \sum_q \left(\frac{p(q)E}{\hbar} \right)^2 \frac{\Gamma}{\Delta\omega^2 + \Gamma^2}, \quad (22)$$

where $\hbar q$ is the electron-hole crystal momentum and V_c the active volume. For practical calculations the product $\mathcal{R}\mathcal{N}_{ij}$ assumes the form [11]

$$\mathcal{R}\mathcal{N}_{ij} = g_0 \ln \left[\frac{N_{ij}}{N_{tr}} \right] v_k N_{p_{ij}} = g_0 \ln \left[\frac{N_{ij}}{N_{tr}} \right] F_{ij}, \quad (23)$$

where N is the total (resonant plus nonresonant) over equilibrium carrier density and the parameters g_0 and N_{tr} are given in terms of the material properties and temperature T .

Due to the fast spatial decay of the radiation profiles away from each lattice center, only the nearest-neighbor interactions $i' = i \pm 1$, $j' = j \pm 1$ in Eqs. (12), (18), and (19) matter for practical purposes. Switching from amplitude E to photon flux F the coupled-cavity rate equations involving the nearest-neighbor interactions are

$$\begin{aligned} \frac{dN_{ij}}{dt} = & \frac{J_{ij}}{ed_w} - \gamma N_{ij} - BN_{ij}^2 - g_0 \ln \left(\frac{N_{ij}}{N_{tr}} \right) F_{ij} \\ & - g_0 \ln \left(\frac{N_{ij}}{N_{tr}} \right) \Lambda \sum_{i'=i\pm 1} \sum_{j'=j\pm 1} F_{i'j'} \\ & - g_0 \ln \left(\frac{N_{ij}}{N_{tr}} \right) Y \sum_{i'=i\pm 1} \sum_{j'=j\pm 1} 2\sqrt{F_{ij}F_{i'j'}} \\ & \times \cos[\varphi_{ij} - \varphi_{i'j'}], \end{aligned} \quad (24)$$

$$\begin{aligned} \frac{dF_{ij}}{dt} = & v_g \zeta g_0 \ln \left(\frac{N_{ij}}{N_{tr}} \right) F_{ij} - v_g \alpha F_{ij} + v_g \zeta g_0 \Lambda \\ & \times \sum_{i'=i\pm 1} \sum_{j'=j\pm 1} \ln \left(\frac{N_{i'j'}}{N_{tr}} \right) F_{i'j'} + v_g \zeta g_0 Y \\ & \times \sum_{i'=i\pm 1} \sum_{j'=j\pm 1} \left[\ln \left(\frac{N_{ij}}{N_{tr}} \right) + \ln \left(\frac{N_{i'j'}}{N_{tr}} \right) \right] \\ & \times \sqrt{F_{ij}F_{i'j'}} \cos[\varphi_{ij} - \varphi_{i'j'}], \end{aligned} \quad (25)$$

$$\begin{aligned} \frac{d\varphi_{ij}}{dt} = & v_g \zeta \frac{g'_0}{2} \ln\left(\frac{N_{ij}}{N_{tr}}\right) + v_g \zeta \frac{g'_0}{2} \Lambda \sum_{i'=i\pm 1} \sum_{j'=j\pm 1} \ln\left(\frac{N_{i'j'}}{N_{tr}}\right) \\ & + v_g \zeta \frac{g_0}{2} Y \sum_{i'=i\pm 1} \sum_{j'=j\pm 1} \left[\ln\left(\frac{N_{ij}}{N_{tr}}\right) \right. \\ & \left. + \ln\left(\frac{N_{i'j'}}{N_{tr}}\right) \right] \sqrt{\frac{F_{i'j'}}{F_{ij}}} \sin[\varphi_{ij} - \varphi_{i'j'}], \end{aligned} \quad (26)$$

where $J_{i,j}$ is the drive current density, γ is the nonradiative recombination factor, g_0 is the gain coefficient, N_{tr} is the transparency density, $\zeta \approx d_w/L_c$ is the gain confinement factor, and $\alpha = -\ln R_c/2L_c$ is the loss coefficient, where R_c includes diffraction, scattering, and reflection losses [12]. The coupling strength between the nearest sites is parametrized by the geometrical overlap factor,

$$\Lambda_{\pm 1} \equiv \Lambda = \frac{1}{\pi w^2} \int_0^{2\pi} d\theta \int_0^a dr r U(\mathbf{r}) \chi(\mathbf{r}) U(\mathbf{r} - \mathbf{b}), \quad (27)$$

$$Y_{\pm 1} \equiv Y = \frac{1}{\pi w^2} \int_0^{2\pi} d\theta \int_0^a dr r U^2(\mathbf{r}) \chi(\mathbf{r} - \mathbf{b}), \quad (28)$$

depending on the active radius a , cavity separation b , and mode waist w , and normalized so that $\Lambda = 1$ for $b = 0$. Substituting the fundamental mode profile $U_{00}(\mathbf{r}) = \sqrt{2/\pi w^2} \exp(-r^2/w^2)$ into Eqs. (27) and (28) and integrating over cylindrical coordinates³ yields

$$Y_{x,y} = 4e^{-b^2_{x,y}/w^2} \frac{1}{w^2} \int_0^a d\rho \rho e^{-2\rho^2/w^2} \mathcal{I}_0(2b_{x,y}\rho/w^2), \quad (29)$$

$$\Lambda_{x,y} = 4e^{-2b^2_{x,y}/w^2} \frac{1}{w^2} \int_0^a d\rho \rho e^{-2\rho^2/w^2} \mathcal{I}_0(4b_{x,y}\rho/w^2). \quad (30)$$

Because of the very short axial cavity length (much smaller than the beam diffraction length) we have employed the zero-mode curvature at the waist $z = 0$. We have also generalized the result for rectangular lattices with $b_x \neq b_y$.

Intercavity coupling strengths depend primarily on the ratio of cavity center separation b to the $1/e^2$ mode waist w . Also, for given b/w , there is a weaker dependence on the cavity separation to diameter ratio b/a (where $b/a = 2$ corresponds to cavities with touching active areas and $b/w = 2$ to cavities with touching mode waists). A comparison between Λ and Y vs b/a is shown in Fig. 3(a) for fixed $a/w = 1$. Coupling strengths diminish rapidly with increasing separation and Λ is always smaller, $O(Y^2)$. Figure 3(b) plots Y vs separation b/a for various relative waist sizes a/w . Figure 3(c) plots Y vs b/w at various cavity separations b/a .

³Using $(\mathbf{r} - \mathbf{b}_x)^2 = (x - b_x)^2 + y^2$, $(\mathbf{r} - \mathbf{b}_y)^2 = (y - b_y)^2 + x^2$, and converting to $x = \rho \cos \phi$, $y = \rho \sin \phi$.

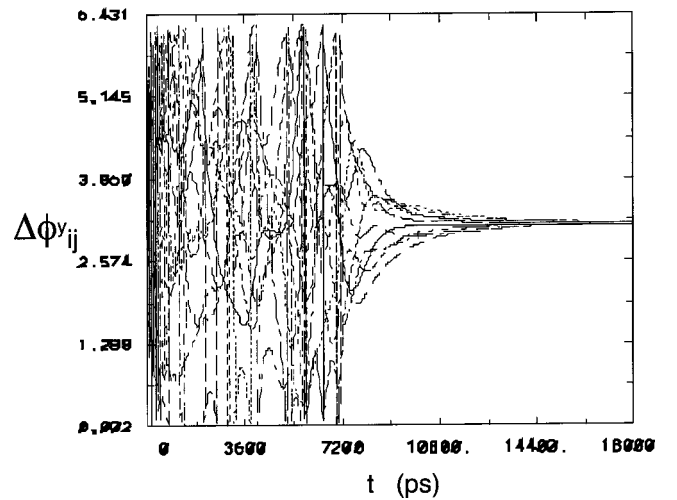
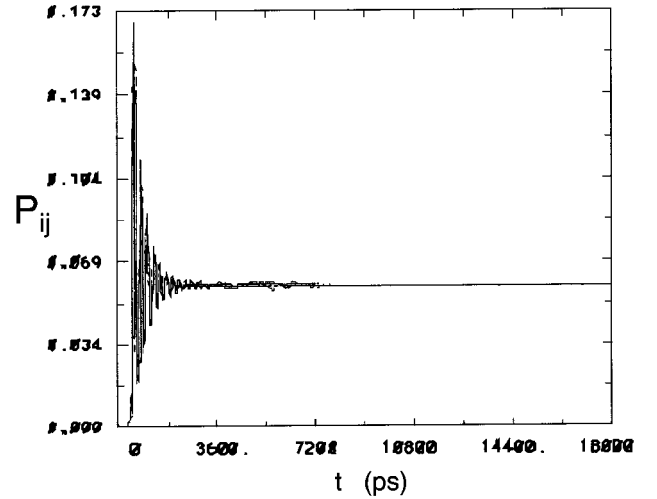


FIG. 4. Spontaneous phase lock in a 1D 1×12 periodic array from uniformly distributed random initial conditions and for constant bias current $I \approx 1.66I_{th}$. (a) Circulating cavity power. (b) Phase difference among adjacent cavities. Intercavity coupling strength $Y = 0.0011$.

In general, for separations $b/w > 2$ we have $\Lambda \approx Y^2 \ll Y \ll 1$, and the phase-dependent Y terms dominate.

IV. MODE-LOCKED ARRAYS

The description of interacting VCSEL arrays by coupled differential equations (24)–(26) greatly reduces simulation time and opens the door for fast and effective numerical studies of generic array behavior. First we investigate the existence of collective steady states under a uniform $J_{ij}(r) = J_0$, constant in time current, which turns on everywhere at $t = 0$. Equations (24)–(26) are integrated starting from random initial conditions for the carrier density and radiation intensity in each cavity. Spontaneous steady state with uniform amplitude F usually develops shortly after, as shown in the example runs in Figs. 4(a) and 5(a), respectively, for a 1D 1×12 and a 2D 5×5 array. Figures 4(b) and 5(b), respectively, show the corresponding evolution of the phase difference among neighbors, $\Delta\varphi_i \equiv \varphi_i - \varphi_{i-1}$, for each lattice site

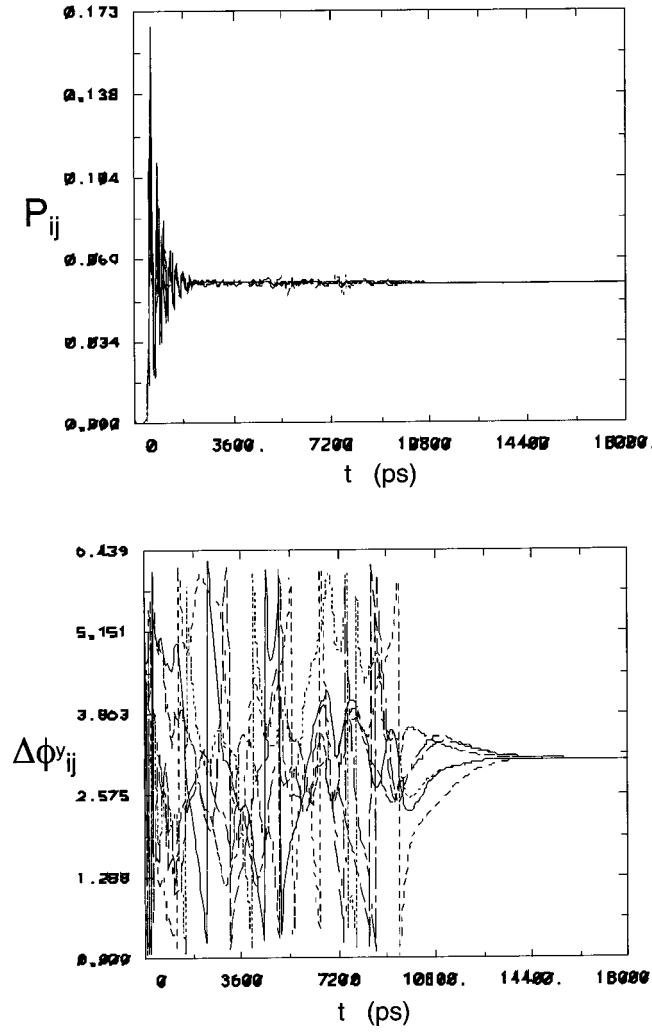


FIG. 5. Spontaneous phase lock in a 2D 5×5 periodic array from uniformly distributed random initial conditions and for constant bias current $I \approx 1.66I_{th}$. (a) Circulating cavity power. (b) Phase difference among adjacent cavities. Intercavity coupling strength $Y = 0.0007$.

array. Clearly a phase-locked state is reached with constant and *equal* phase difference between nearest sites. The radiation amplitude and carrier density settle to the same value in all sites. Thus, a VCSEL array with close site coupling is naturally phase locked. The time lapsed before phase locking depends on the coupling strength, and is shorter for higher Λ . Analytic steady-state solutions for the density and amplitude are obtained from the zeros of Eq. (24) and (25). A constant phase condition $d\varphi_{ij}/dt = 0$ at each site cannot be met (except in trivial cases). Instead we look for a constant phase difference among neighboring sites, manifesting mode locking. The phase difference evolution is obtained by subtracting Eqs. (26) among any two neighboring sites for $\Delta_{\pm}^x \varphi_{i,j} \equiv \varphi_{i,j} - \varphi_{i\pm 1,j}$ and $\Delta_{\pm}^y \varphi_{i,j} \equiv \varphi_{i,j} - \varphi_{i,j\pm 1}$. Because of lattice periodicity $\Delta_{\pm}^x \varphi_{i,j}$ and $\Delta_{\pm}^y \varphi_{i,j}$ are related through the Bloch condition, thus it is sufficient to record $\Delta_{-}^y \varphi_{i,j}$, given by

$$\begin{aligned} \frac{d\Delta\varphi_{ij}}{dt} = & v_g \zeta \frac{g'_0}{2} \ln\left(\frac{N_{ij}}{N_{i,j-1}}\right) \\ & + v_g \zeta \frac{g'_0}{2} \Lambda \sum_{i'=i\pm 1} \sum_{j'=j\pm 1} \ln\left(\frac{N_{i'j'}}{N_{i'j'-1}}\right) \\ & + v_g \zeta \frac{g_0}{2} Y \sum_{i'=i\pm 1} \sum_{j'=j\pm 1} \left\{ \ln\left(\frac{N_{ij}N_{i'j'}}{N_{tr}^2}\right) \right. \\ & \times \sqrt{\frac{F_{i'j'}}{F_{ij}}} \sin \Delta\varphi_{ij} - \ln\left(\frac{N_{i,j-1}N_{i',j'-1}}{N_{tr}^2}\right) \\ & \left. \times \sqrt{\frac{F_{i'j'-1}}{F_{i,j-1}}} \sin \Delta\varphi_{i,j-1} \right\}. \end{aligned} \quad (31)$$

Notice that a uniform distribution of amplitudes and densities $N_{ij} = \text{const}$, $F_{ij} = \text{const}$ over the array yields a mode-locked steady state $d\Delta\varphi_{ij}/dt = 0$ for *any* uniform phase difference between adjacent sites.

Of the most general set of steady states [zero right-hand side of Eqs. (24), (25), and (31)] we are interested in the uniform solutions subset, with constant density and amplitude over the array given, respectively, by $N_{ij} = N_o$ and $F_{ij} = F_o = (\Lambda - \tilde{\gamma}N_o)/(\alpha/\zeta)$, where

$$N_o = N_{tr} \exp\left\{ \frac{\alpha/\zeta}{g_0[1 + 4\Lambda + 4Y \cos \Delta\varphi_o^x + 4Y \cos \Delta\varphi_o^y]} \right\}, \quad (32)$$

$$\begin{aligned} F_o = & \zeta \frac{\gamma}{\alpha} \left\{ \frac{J_o}{ed_w \gamma} - \frac{\tilde{\gamma}}{\gamma} N_{tr} \right. \\ & \left. \times \exp\left[\frac{\alpha/\zeta}{g_0[1 + 4\Lambda + 4Y \cos \Delta\varphi_o^x + 4Y \cos \Delta\varphi_o^y]} \right] \right\}. \end{aligned} \quad (33)$$

Any value of $\Delta\varphi_o^x$, $\Delta\varphi_o^y$, yields a steady state. Periodic boundaries every N and M sites, and the Bloch requirement for the solutions impose $\Delta\varphi_o^x = \mathbf{K} \cdot \mathbf{b}_x = m(2\pi)/N$ and $\Delta\varphi_o^y = \mathbf{K} \cdot \mathbf{b}_y = n(2\pi)/M$ corresponding to wave vectors $\mathbf{K} = (K_m, K_n)$ of the inverse lattice. Henceforth we will label the steady state $\Delta\varphi$ by the corresponding Brillouin-zone vector \mathbf{K}_{mn} ,

$$\Delta\varphi_{mn} \equiv (\Delta\varphi_o^x, \Delta\varphi_o^y) = (K_m b, K_n b). \quad (34)$$

For convenience we also define the lattice dispersion factor

$$\begin{aligned} \Xi(\mathbf{K}_{mn}) = & 1 + 4\Lambda + 4Y \cos \Delta\varphi_o^x + 4Y \cos \Delta\varphi_o^y = 1 + 4\Lambda \\ & + 4Y \cos K_m b + 4Y \cos K_n b, \end{aligned} \quad (35)$$

which will enter subsequent relations. Plots of N_o and F_o vs $\Delta\varphi_{mn}$ for various coupling strengths Y (and Λ set to Y^2) are shown in Fig. 6 for given $\alpha = 1347 \text{ cm}^{-1}$, $g_0 = 1117 \text{ cm}^{-1}$, $\gamma = 1.882 \times 10^9 \text{ sec}^{-1}$, $B = 3 \times 10^{-11} \text{ sec}^{-1} \text{ cm}^3$, $d_w = 30 \text{ nm}$, and current $I = 3.090 \text{ mA}$ over active radius $a = 3 \mu\text{m}$.

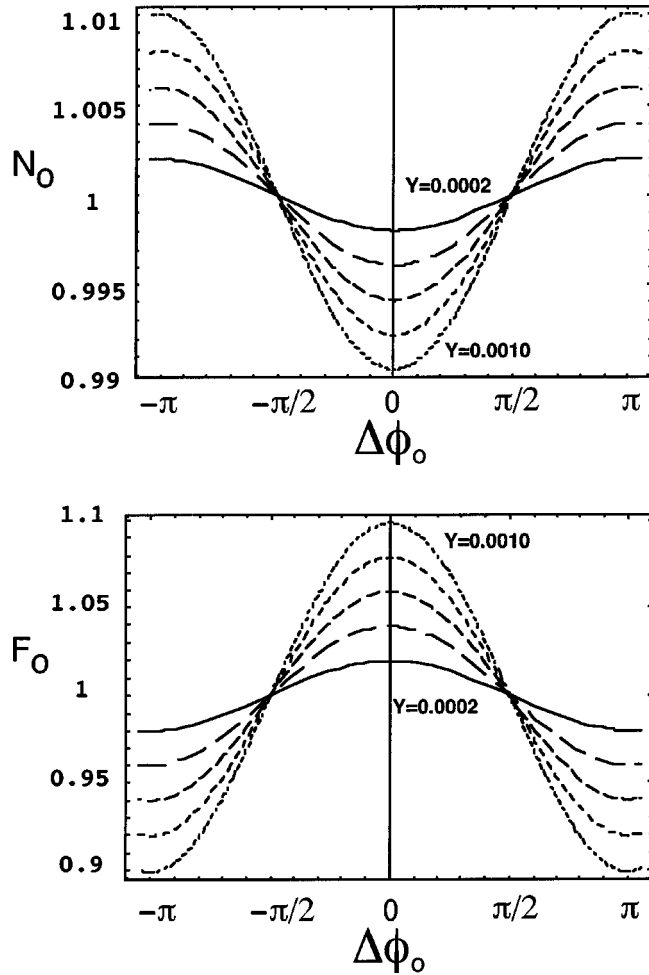


FIG. 6. Dependence of steady-state quantities on phase-lock difference and coupling strength. (a) Density, normalized to stand alone lasing threshold N_0 . (b) Radiation intensity, normalized to stand alone saturation F_0 .

It appears that the $\Delta\varphi_{x,y} \rightarrow \pi$ steady state (antiphasing among near sites) is favored for high N and M regardless of the initial conditions. (For even values of M or N , $\Delta\varphi_{x,y}$ settles to the nearest to π allowed $2\pi m/(M-1)$, namely, $m = M/2 \pm 1$, with equal probability.) Figure 7 shows the final intensity profiles and radiation envelopes of a 5×5 array with periodic boundary conditions, starting from random initial phases $\Delta\varphi$ distributed in the $(0-\pi)$ interval and with coupling strength $Y=0.0007$. The snapshot at 18 ns shows the antiphased configuration where the array remained after a spontaneous mode locking occurred at 12 ns from launching. The tendency for antibiasing is better demonstrated in Fig. 8 showing the evolution of an array originally prepared near the steady-state values (32),(33) corresponding to $K_x b = \pi/2$ and $K_y b = 3\pi/2$. After an initial quiescent period, an instability erupts that relaxes to the preferred steady state with $K_x b = K_y b = \pi$. In nonlinear dissipative systems, a given final steady state can be reached from an entire set of initial conditions (*basin of attraction*) due the *collapsing* of the phase-space volume. It will be subsequently shown that steady states corresponding to any of the $\Delta\varphi_{mn}$ values (34) are stable against perturbations and should occasionally oc-

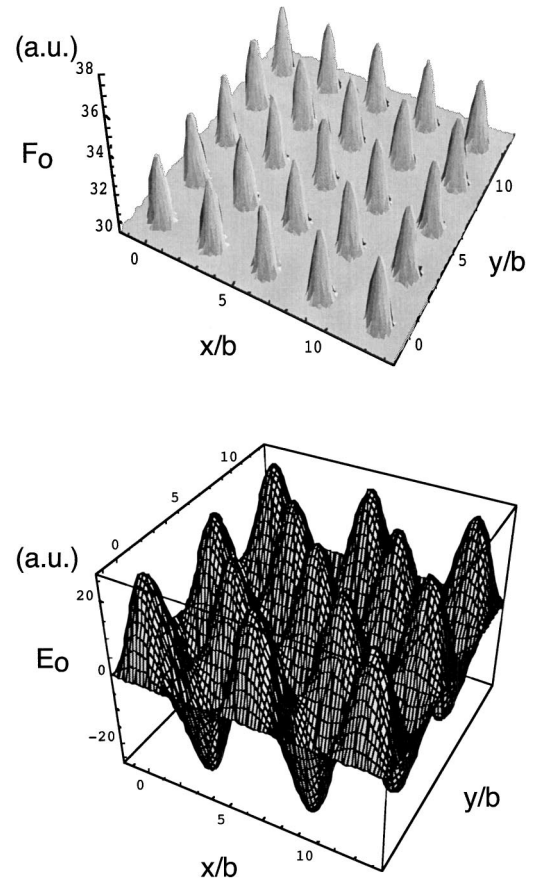


FIG. 7. Snapshot of the radiation profile over the 5×5 array of Fig. 5 at $t=18$ ns. (a) Radiation intensity. (b) Radiation amplitude. The antiphase locking is evident.

cur as final steady-state configurations. An explanation of the preference for the π phasing will be given in Sec. V, drawing formal analogy with the minimum energy of a mechanical system with friction.⁴ We will also see that for increasingly stronger coupling the system first evolves into (quasi) periodic limit cycles, whereby $\Delta\varphi_{ij}$, \mathcal{E}_{ij} , and N_{ij} undergo coherent oscillations about some average values, and finally exhibit chaotic behavior.

Numerical simulations of finite-size arrays, performed by removing the appropriate coupling terms at the boundary lattice sites, also resulted in phase-locked states. Since finite boundaries destroy periodicity, the phase shift among adjacent sites is not uniform and given by the zeros of the full $3N \times 3M$ tridiagonal system. Finite large size 2D arrays may also accommodate a coherent phase lock into 1D surface states, forming boundary layers. It was finally verified that in the zero-coupling limit the phase differences among neighbors settle to constant in time, but random values. Since the same steady-state density and intensity values result for identical cavities we also have $d\varphi_i/dt - d\varphi_j/dt \rightarrow 0$ among any

⁴The approach may lack general validity since we are not dealing with a system in thermodynamic equilibrium, relaxing to a minimum energy, but with a steady state maintained under external drive and tending towards minimum *entropy production rate*.

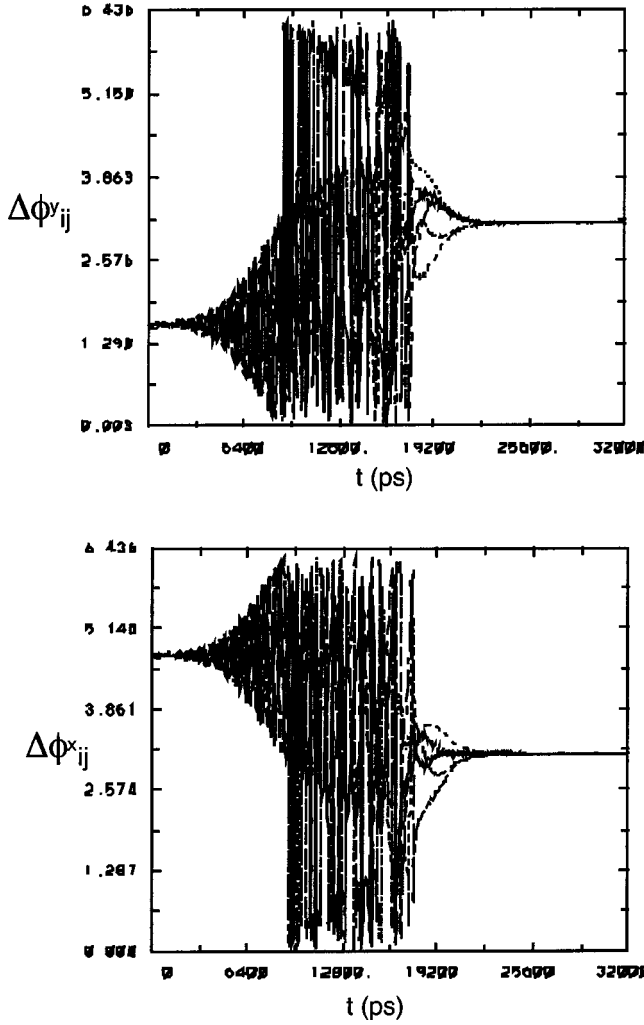


FIG. 8. Spontaneous transition to the antiphased configuration in a 5×5 periodic array initiated with coherent initial phases $\Delta\varphi_1 = \pi/2$, $\Delta\varphi_2 = 3\pi/2$ and the same density and amplitudes. (a) Circulating cavity power. (b) Phase difference among adjacent cavities. Intercavity coupling strength $Y=0.0007$ and the rest of parameters as in Fig. 5.

i, j , hence the final constant phase difference $\Delta\varphi_{ij}$ merely reflects the difference in initial conditions.

V. COLLECTIVE LATTICE OSCILLATIONS AND STABILITY

Further understanding of the array behavior results by analyzing the stability of small oscillations around the steady state. Assume for simplicity that a steady state with $\Delta\varphi_{ij} = \Delta\varphi_o$, $\mathcal{E}_{ij} = \mathcal{E}_o$, $N_{ij} = N_o$ has been reached and examine the evolution of small perturbations about these values. According to the Bloch theory, collective modes over a periodic lattice must also be of the form

$$\delta A = A_o e^{\lambda t} \sum_{i,j} e^{\kappa \cdot \mathbf{R}_{ij}}, \quad (36)$$

where δA stands for either density or radiation amplitude. Equation (36) also implies that the perturbed phase difference among any adjacent sites is fixed, shifting from the equilibrium value to $\Delta\varphi' \rightarrow \Delta\varphi_o + \kappa \Delta \mathbf{R}_{ij} = \mathbf{K} \cdot \mathbf{b} + \kappa \mathbf{b}$. Replacing independent phase shifts by a periodic phase difference over lattice sites manifests the transition to collective behavior with long-range coherence.⁵ The description resembles the dynamic behavior of a periodic spring-coupled mass system, a model finding wide applications in lattice dynamics. Due to the periodicity, linearization of Eqs. (24)–(26) about any site leads to identical stability equations. Picking an arbitrary $\mathbf{R}_{ij} = \mathbf{R}_o$, expanding around equilibrium and the use of Eq. (36) yields the following equation for perturbations about the steady state:

$$\frac{d}{dt} \begin{pmatrix} \delta N \\ \delta F \end{pmatrix} = \lambda \begin{pmatrix} \delta N \\ \delta F \end{pmatrix} = \begin{pmatrix} -D_{NN} & D_{NF} \\ D_{FN} & -D_{FF} \end{pmatrix} \begin{pmatrix} \delta N \\ \delta F \end{pmatrix}. \quad (37)$$

The elements $D_{XY} \equiv \partial(\dot{X})/\partial Y$ with X, Y being either of $N, \mathcal{E}, \Delta\varphi$ are found from the rhs of Eqs. (24)–(26) at steady state (Appendix B),

$$D_{NN} = \gamma + 2BN_o + \frac{g_0 F_o}{N_o} \frac{\alpha/\zeta}{g_0 \ln(N_o/N_{tr})}, \quad (38)$$

$$D_{FF} = v_g \zeta g_0 \ln(N_o/N_{tr}) 2Y \times [\cos K_m b - \cos \kappa'_x b + \cos K_n b - \cos \kappa'_y b], \quad (39)$$

$$D_{NF} = -\alpha/\zeta + g_0 \ln(N_o/N_{tr}) 2Y \times [\cos K_m b - \cos \kappa'_x b + \cos K_n b - \cos \kappa'_y b], \quad (40)$$

$$D_{FN} = v_g \zeta \frac{g_0 F_o}{N_o} \frac{\alpha/\zeta}{g_0 \ln(N_o/N_{tr})}, \quad (41)$$

where $\kappa'_{x,y} = K_{m,n} + \kappa_{x,y}$. Note (Appendix B) that the linearization of the phase difference equation (31) yields $D_{\Phi N} = D_{\Phi F} = D_{\Phi\Phi} = 0$, consistent with the freedom to choose a fixed, arbitrary phase difference κb among adjacent sites. Diagonalization of

$$\det \begin{vmatrix} -D_{NN} - \lambda & D_{NF} \\ D_{FN} & -D_{FF} - \lambda \end{vmatrix} = 0 \quad (42)$$

yields the eigenvalue equation

$$\lambda^2 + (D_{NN} + D_{FF})\lambda + (D_{NN}D_{FF} - D_{NF}D_{FN}) = 0, \quad (43)$$

whereby letting $\Theta = \lambda_{1,2}$ yields the dispersion relation for collective modes over the cavity lattice, written in the form

⁵During the evolution towards a steady state, or in a situation far from equilibrium, the phase differences among sites are treated as independent variables according to Eq. (26) or (31).

$$\Theta(\kappa'; K) = -\Gamma(\kappa'; K) \pm i\Omega(\kappa'; K) \sqrt{1 - \Gamma^2(\kappa'; K)/\Omega^2(\kappa'; K)}, \quad (44)$$

where $\Omega \equiv \sqrt{D_{NF}|D_{FN}| - D_{FF}D_{NN}}$ and $\Gamma \equiv (D_{NN} + D_{FF})/2$. The obtained dispersion branches form the propagating bands of an active photonic lattice. They depend on the steady-state period \mathbf{K} and the total perturbation wave number

$$\kappa' = \mathbf{K} + \kappa. \quad (45)$$

Using the steady-state values in the rhs of $\Omega(\kappa)$ we obtain

$$\Omega(\kappa'; K) = \hat{\Omega}(K) \left\{ 1 - 2YZ_o \times \frac{\cos K_m b - \cos \kappa'_x b + \cos K_n b - \cos \kappa'_y b}{\Xi(\mathbf{K})} \right\}^{1/2}, \quad (46)$$

where $\hat{\Omega} = \sqrt{D_{NF}|D_{FN}|}$ is the coupled-cavity oscillation frequency

$$\hat{\Omega}(K) = \Omega_o \sqrt{\Xi(K)}, \quad (47)$$

Ω_o being the oscillation (relaxation) frequency for an isolated cavity,

$$\Omega_o = \sqrt{v_g \alpha \frac{g_0 F_o}{N_o}} = \sqrt{\gamma v_g \alpha \frac{N_J/N_o - 1}{\ln(N_o/N_{tr})}}. \quad (48)$$

The factor $Z_o = 1 + 1/\Xi + \ln(N_o/N_{tr})\zeta\tilde{\gamma}N_o/(F_o\alpha)$. The oscillation decay rate Γ is related to the stimulated $\gamma_s = g_0 F_o/N_o$ and the total nonstimulated $\tilde{\gamma} = \gamma + 2BN_o$ decay rates by

$$\Gamma(\kappa') = \frac{1}{2} \tilde{\gamma} \left[1 + \frac{\gamma_s}{\tilde{\gamma}} \Xi(\mathbf{K}) + 2Y \frac{v_g \alpha \cos K_m b - \cos \kappa'_x b + \cos K_n b - \cos \kappa'_y b}{\tilde{\gamma} \Xi(\mathbf{K})} \right]. \quad (49)$$

In the $\Lambda = Y = 0$ uncoupled limit, Γ tends to the single-cavity decay rate $\Gamma_o = (\tilde{\gamma} + \gamma)/2$ from the combined nonradiative and stimulated emission. For very small coupling Γ is much smaller than Ω , scaling as $\Gamma/\Omega \approx \Gamma_o/\Omega_o \approx \sqrt{\gamma/v_g \zeta \alpha} \ll 1$, so one may set the square root in Eq. (44) to unity. Plots of Ω and Γ vs κb for given $Y = 0.0003$ and various $\Delta\varphi_o = Kb$ (where again $K_x = K_y$) are shown in Fig. 9. Here we have set $\kappa'_x = \kappa'_y = \kappa'$ to limit the parameter space. For any given Ω and K Eq. (46) yields two solutions κ_1, κ_2 corresponding to the roots of $\cos Kb - \cos(K + \kappa)b = C_\Omega$. Figure 10 shows the general dispersion Ω over the κ_x, κ_y space for given Kb .

An excited lattice wave of the real wave number κ' is a stable perturbation of real frequency $\Omega(\kappa')$ that decays in time with decay rate $\Gamma(\kappa')$. However, cross-coupling cor-

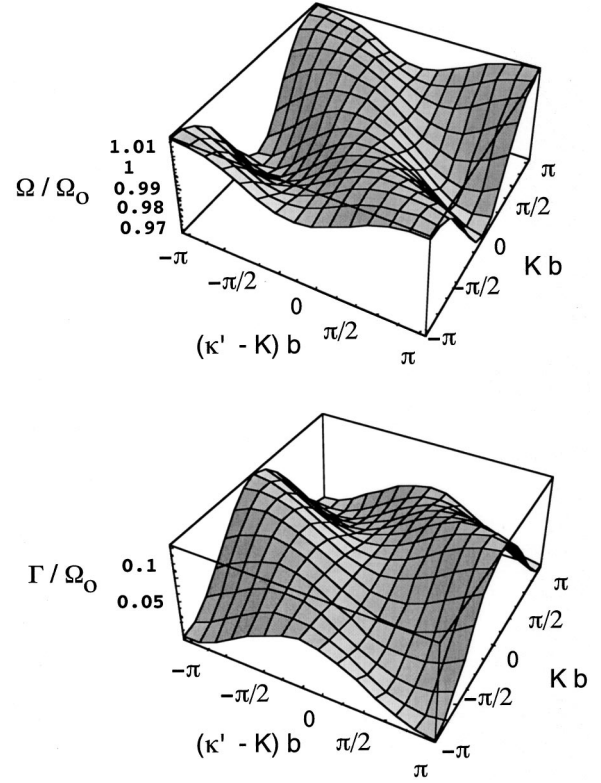


FIG. 9. Dispersion relation for the modulation waves at coupling strength $Y = 0.0002$. 3D plots of the (a) frequency $\Omega \approx \text{Im } \Theta$ and (b) decay rate Γ (normalized over the isolated cavity Ω_o) over wave-number space K and $\kappa = \kappa' - K$.

rections soon become important at low coupling strength $\Lambda \sim Y \ll 1$ due to the factor $v_g \alpha / \tilde{\gamma} \gg 1$ multiplying the last coupling term in Eq. (49). The large size of this term reflects the fact that the radiation growth rate is the algebraic sum of large numbers, thus a small imbalance caused by a phase difference among perturbed adjacent densities has a big effect in the growth rate. When Y exceeds a stability threshold,

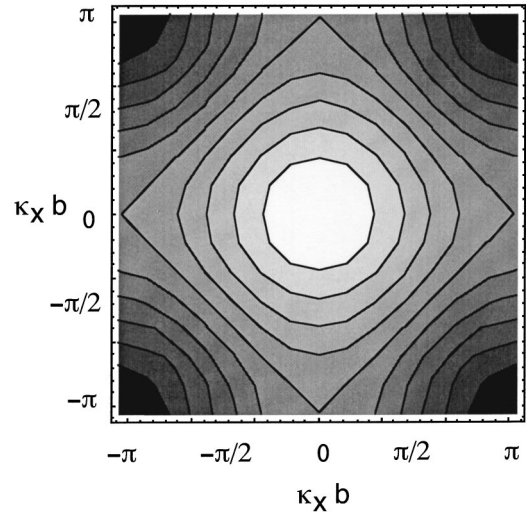


FIG. 10. Contour plots of the frequency $\Omega \approx \text{Im } \Theta$ (normalized over the isolated cavity Ω_o) over the 2D first Brillouin zone $\kappa_x \neq \kappa_y$ for fixed $Y = 0.0002$ and $K = \pi$.

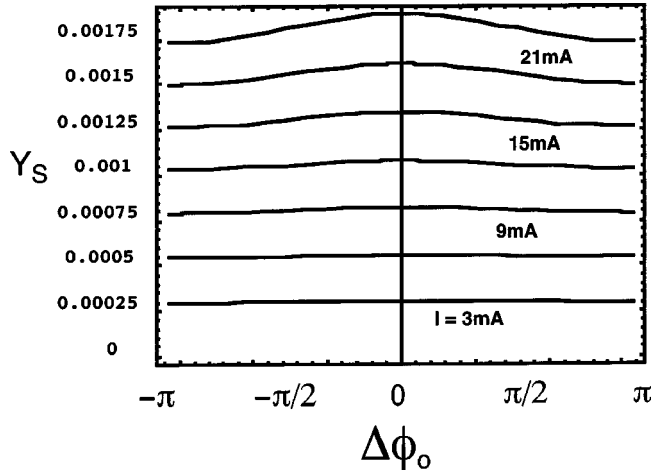


FIG. 11. Loss of fixed-phase stability threshold Y_S vs steady state $\Delta\varphi_o$ for various drive current values ($I_{th}=1.81$ mA).

$$Y_S \equiv \frac{1}{4} \frac{\tilde{\gamma}}{v_g \alpha} \Xi(\Delta\varphi_o) \left(1 + \frac{\gamma_s}{\tilde{\gamma}} \Xi(\Delta\varphi_o) \right), \quad (50)$$

Γ turns negative, and perturbations within the range

$$\kappa b \leq \cos^{-1} \left[\cos \Delta\varphi_o + \frac{Y_S}{Y} \right] - \Delta\varphi_o, \quad (51)$$

$$\cos \Delta\varphi_o \leq 1 - \frac{Y_S}{Y} \quad (52)$$

become *unstable*. [Relation (52) yields the $\Delta\varphi_o$ range for which inequality (51) admits solutions for κb .] The stability threshold Y_S is plotted in Fig. 11 vs $\Delta\varphi_o$. Y_S is minimum for $\Delta\varphi_o = \pi$ and phase locking with $\Delta\varphi_o = \pi$ is destabilized first to long-wavelength fluctuations $\kappa b \ll 1$; $\Delta\varphi_o = 0$ is the last to lose stability, for $Y \gg Y_S^* \equiv Y_S(0)$ due to Eq. (52). No phase locking with fixed $\Delta\varphi_o$ between cavities exists above Y_S^* , since there is always an unstable range of excited fluctuations for *any* value of $\Delta\varphi_o$. A new coherent pattern of behavior emerges whereby the amplitudes and relative phase differences settle into a periodic orbit $\Delta\tilde{\varphi}_o(t)$. The old (and now unstable) fixed points $\Delta\varphi_o$ lie inside this orbit. The new behavior is illustrated in Fig. 12 showing the time evolution $F_{ij}(t)$ and $\Delta\varphi_{ij}(t)$ for the same parameters as Fig. 5, except that here $Y=0.0009 > Y_S$. The stable “attracting” orbit is better observed in Fig. 13(a) by plotting $F_{ij}(t)$ against $N_{ij}(t)$ for the boxed area data of Fig. 12. Remarkably, the plot $\Delta\varphi_{ij}^x(t)$ against $\Delta\varphi_{ij}^y(t)$ in Fig. 13(b) shows that the phase differences in the x and y array directions remain mutually equal as they change in time. The phase does not enter the regime $\Delta\varphi(t) > \cos^{-1}(1 - Y_S/Y)$, where fixed phase solutions are, in principle, possible due to Eq. (52). The same phase-space trajectory occurs for all cavities, and perturbations away from that cycle converge back to it. It represents a generic example of Hopf bifurcation, where the loss of stability of a fixed point leads to a stable limit cycle. Pushing the coupling Y even higher leads to cycles of increasing complexity and longer periods until chaotic behavior settles in.

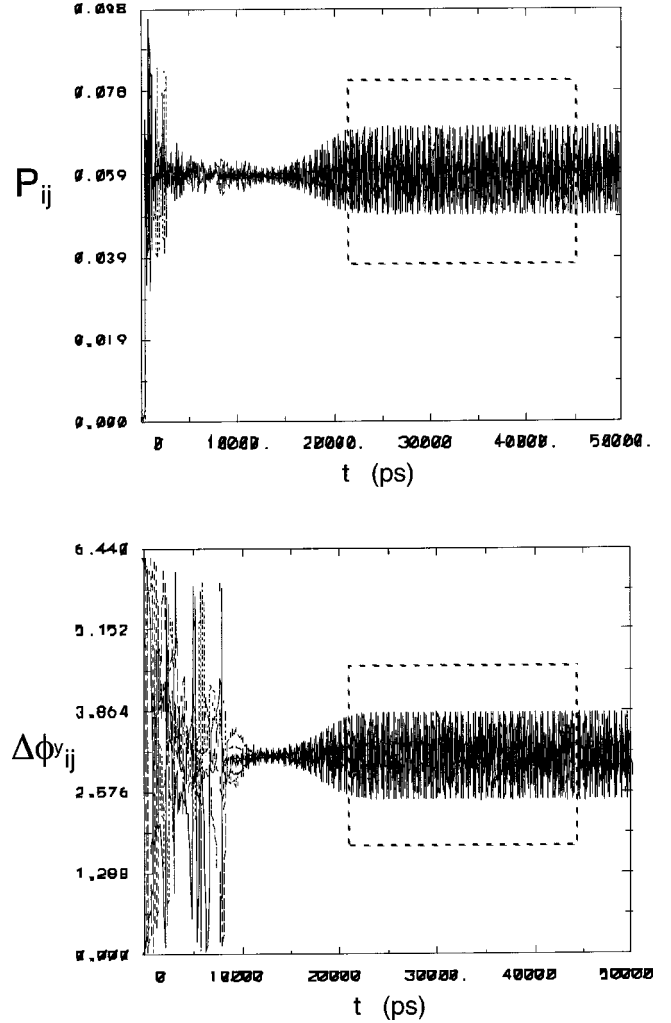


FIG. 12. Spontaneous transition to a limit cycle behavior in a 5×5 periodic array at coupling strength $Y=0.0009$ and the rest of parameters as in Fig. 5. (a) Circulating cavity power. (b) Phase difference among adjacent cavities.

We will not investigate chaotic behavior in detail. However, the inspection of the dispersion relation (44) shows that a transition to an absolute instability occurs, crossing the parameter boundary $\Gamma/\Omega > 1$, whereby Θ becomes pure real,

$$\Theta(\kappa'; K) = -\Gamma \left[1 \pm \sqrt{1 - \frac{\Omega^2}{\Gamma^2}} \right] \approx -\Gamma \left[1 \pm \left(1 - \frac{\Omega^2}{2\Gamma^2} \right) \right]. \quad (53)$$

The absolute instability limit Y_{abs} is given, using Eqs. (49) and (46),(47), by

$$Y_{abs} \equiv \frac{\Omega_o \sqrt{\Xi(\mathbf{K})}}{2v_g \alpha} \left(1 - \frac{\gamma + \frac{g_0 F_o}{N_o} \Xi(\mathbf{K})}{2\Omega_o \sqrt{\Xi(\mathbf{K})}} \right). \quad (54)$$

Since $Y_{abs} > Y_S$ we also have $\Gamma < 0$ for $Y > Y_{abs}$, thus both roots in Eq. (53) yield pure exponential growth. For $\gamma_s/\tilde{\gamma}$

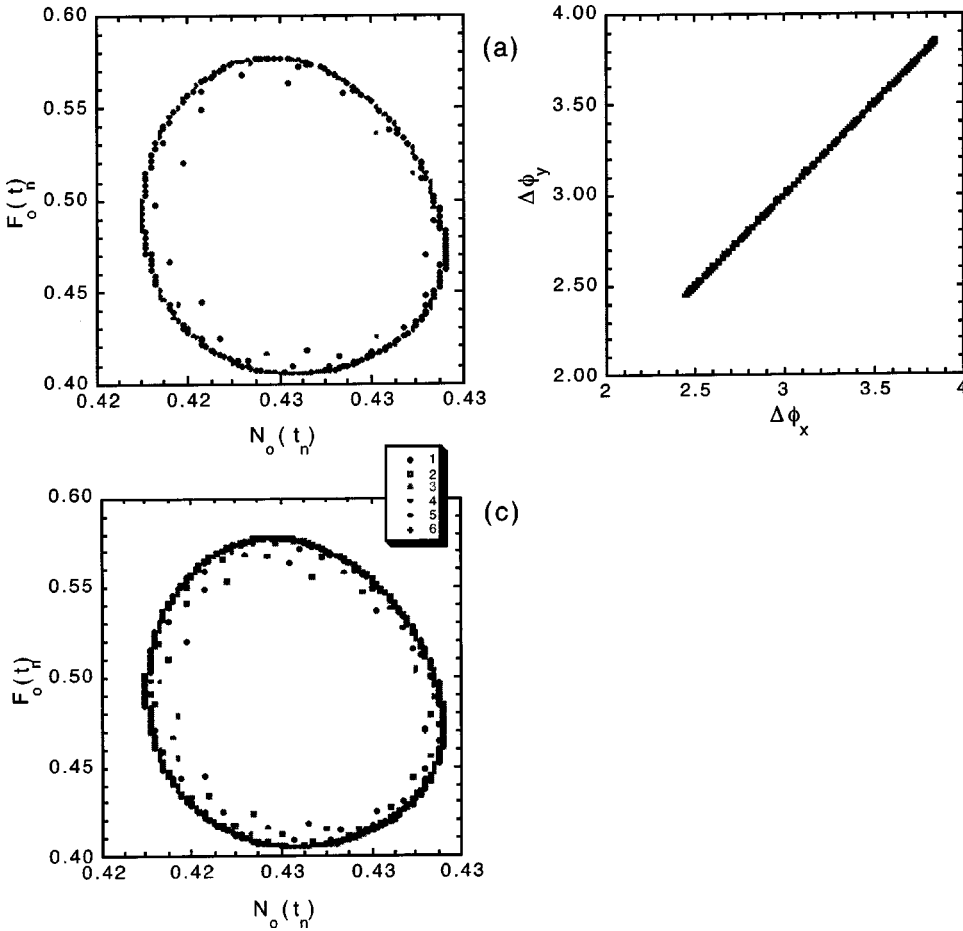


FIG. 13. Parametric plot (“surface of section”) of the limit cycle using the data in the boxed area of Fig. 12. (a) $N_o(t_n)$ vs $F_o(t_n)$ for a given cavity. (b) Phase difference $\Delta\phi_y^x(t_n)$ vs $\Delta\phi_o^y(t_n)$ for a given cavity. (c) Accumulated $N_o(t_n)$ vs $F_o(t_n)$ for all cavities.

<1 the absolute threshold value Y_{abs} is minimum⁶ at $\Delta\varphi_o = 0$ and maximum at $\Delta\varphi_o = \pi$. For $Y > Y_{abs}^* \equiv Y_{abs}(\pi)$ we have $\Gamma/\Omega > 1$ regardless of $\Delta\varphi_o$. While the $Y > Y_s$, $\Gamma > 0$ threshold of the preceding paragraph allows for the existence of stable periodic orbits after the destabilization of the original fixed points, we conjecture (Appendix C) that $\Gamma/\Omega > 1$ implies complete absence of stable coherent orbits, leading to “lattice turbulence.” Figure 14 is a 3D plot of the real part $\text{Re}\Omega$ over the 2D parameter space Y and κ , for given $\Delta\varphi_o = \pi$. The parameter area with $\text{Re}\Omega = 0$ is the absolute instability range; its boundaries in $Y - \Delta\varphi_o$ mark the parameter space boundaries for instability.

So far, we have employed the scaling $\Omega_o/\gamma \approx \sqrt{v_g \alpha}/\gamma \gg 1$ falling within the usual range of manufactured VCSEL parameters. The opposite limit $\Omega_o/\gamma \approx \sqrt{v_g \alpha}/\gamma \ll 1$, regarding combinations of low group velocity and/or very high cavity quality (small $\alpha \approx -\ln R_{cav}$),⁷ is also interesting. In that regime we always have $\Gamma/\Omega > 1$, and Eq. (44) with pure real Θ holds regardless of Y . In addition, we always have $\Gamma > 0$ [the threshold value Eq. (54) for $\Gamma < 0$ now yields $Y_s > 1$, while the overlap factor Y cannot exceed unity], thus both roots correspond to negative Θ meaning pure damping of fluctuations and unconditional stability of the phase-

locked fixed points in the linear coupling regime (Y small.) Figure 15, corresponding to 1/100 of the cavity losses and material gain, and 1/100 of the group velocity, with same other parameters as Fig. 5, exhibits phase-locked behavior at five times higher coupling strength $Y = 0.003$. For typical values γ in the nanosecond range Ω_o must drop well below the gigahertz range to achieve this scaling, evident in the long-time scale of Fig. 15.

VI. EVANESCENT LATTICE WAVES

We have dealt with the behavior of fluctuations of real κ using the dispersion relation (44). It applies to an initial-value problem, following the time evolution from an arbitrary initial superposition of real wave-number modes, whereby all modes subsequently decay in time with rates $\Gamma(\kappa)$. The related boundary-value problem is also of interest, where we specify a boundary condition in time (say, drive selected members of the array) and record evolution in space. A real driving frequency now leads to complex wave numbers $\kappa \rightarrow \kappa + i\eta$ and evanescent waves in space. The decay constant $\eta(\Omega)$ is found by solving Eq. (44) for $\text{Im}\Theta(\kappa + i\eta) = 0$ under given $\Omega = \text{Re}\Theta(\kappa + i\eta)$. For $\Gamma/\Omega \approx \gamma/\Omega_o \ll 1$, and for $Y < Y_s$ (i.e., stable steady state) η is also small; an expansion of $\cos(\kappa b + i\eta b) = \cos(\kappa b)\cosh(\eta b) - i\sin(\kappa b)\sinh(\eta b)$ and letting $\cosh(\eta b) = 1$ yields

⁶The opposite is valid when $\gamma_s/\tilde{\gamma} < 1$.

⁷Large carrier decay rate γ is of little practical interest.

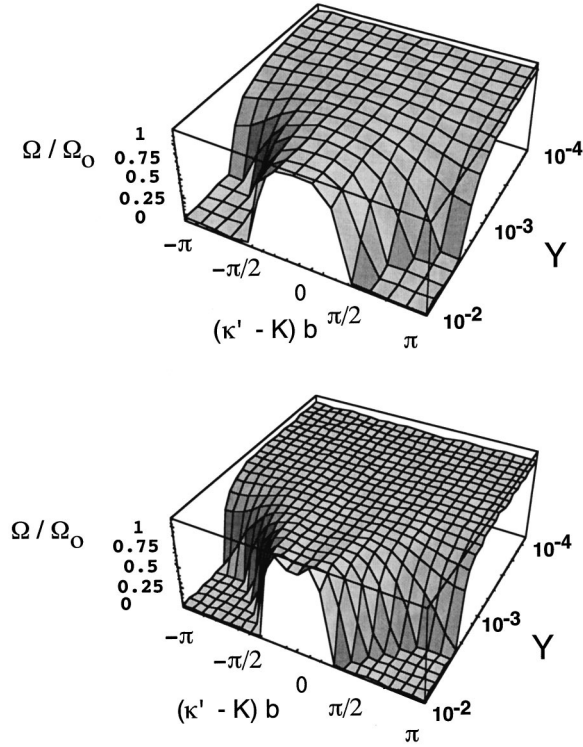


FIG. 14. 3D plots of the frequency $\Omega \approx \text{Im } \Theta$ over the $\kappa = \kappa' - K$ and Y space for (a) $Kb=0$ and (b) $Kb=\pi$. The zero-frequency area marks the absolute instability parameter space (pure real Θ with positive $\text{Re } \Theta = -\Gamma > 0$).

$$\eta = \frac{1}{b} \sinh^{-1} \left\{ \frac{1}{Y} \frac{\bar{\gamma} \Xi(\mathbf{K})}{4\Omega_o Z_o} \right. \\ \left. \times \frac{1 + \frac{\gamma_s}{\bar{\gamma}} \Xi(\mathbf{K}) + 4Y \frac{v_g \alpha \cos \Delta\phi_o - \cos(\Delta\phi_o + \kappa b)}{\Xi(\mathbf{K})}}{\sin[\Delta\phi_o + \kappa b]} \right\}. \quad (55)$$

Figure 16 plots ηb vs κb for various Y values. For the considered parameter values the decay length $l_d \equiv 1/\eta$ is shorter than the lattice spacing $\eta b = b/l_d > 1$. Even so, the induced coherence length for the phase interaction is much longer. Figure 17 plots the space-time evolution of a 21-cavity periodic 1D array, where all cavities are held at constant bias $I = 1.67I_{th}$, while the central cavity $j=11$ is excited by a superimposed modulated bias of amplitude $\pm 0.12I_{th}$ near the resonant array frequency $\Omega = 1.32 \times 10^{10}$ rad/s. Evanescent waves propagating away from the center are obvious in Fig. 17. The intensity amplitude plot, Fig. 17(a), shows rapid decay of the excited amplitudes across only few sites of the array span. However, a persistent long-range coherence is evident from the phase plot of Fig. 17(b), showing the slow oscillating phase φ (not the phase difference $\Delta\varphi$) in each site. Wave fronts propagating over the entire array at the group velocity $y = v_g t$ are evident, hence the coherence length exceeds the amplitude decay distance. We found that the period is not equal to π , i.e., the phase difference among adjacent

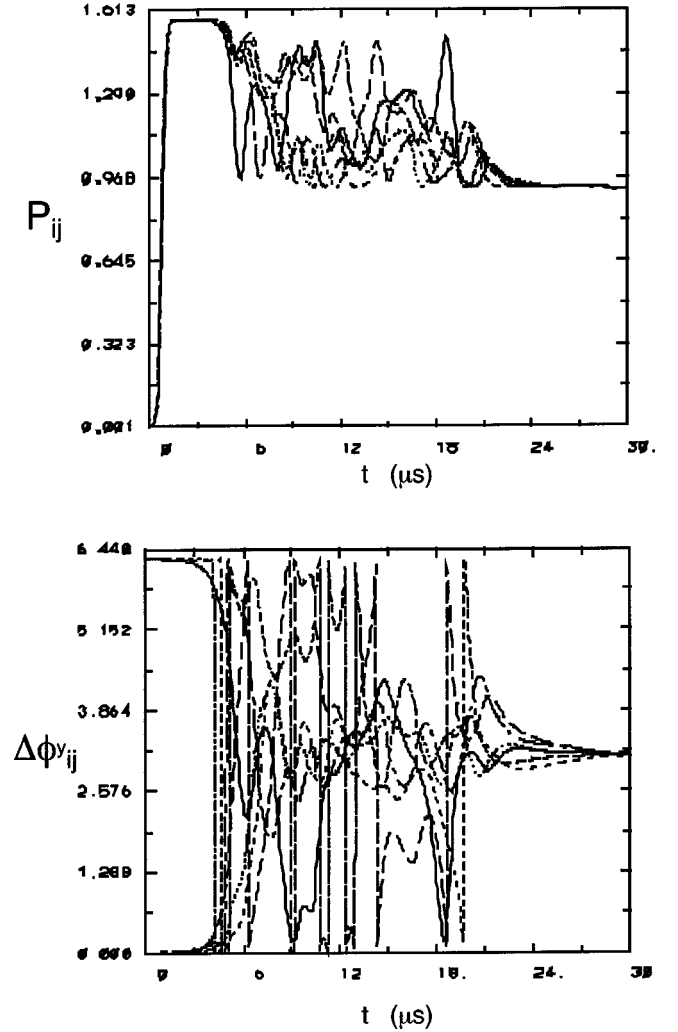


FIG. 15. Spontaneous phase lock for high intercavity coupling strength $Y=0.003$ in a 2D 5×5 periodic array in the $\Omega_o < \gamma$ regime. (a) Circulating cavity power. (b) Phase difference among adjacent cavities. Parameters are the same as in Fig. 5, except that the gain and loss coefficients and the group velocity are reduced by 1/100. Uniformly distributed random initial conditions are used.

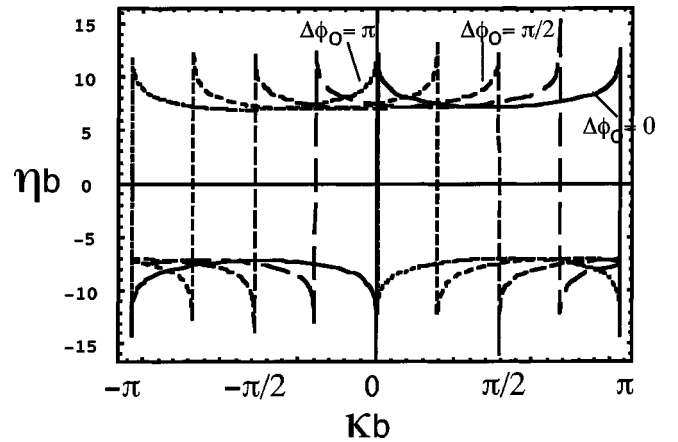


FIG. 16. Plot of decay constant ηb vs the real wave number κb for various values of the steady state $\Delta\phi_o$ for coupling strength $Y = 0.0011$.

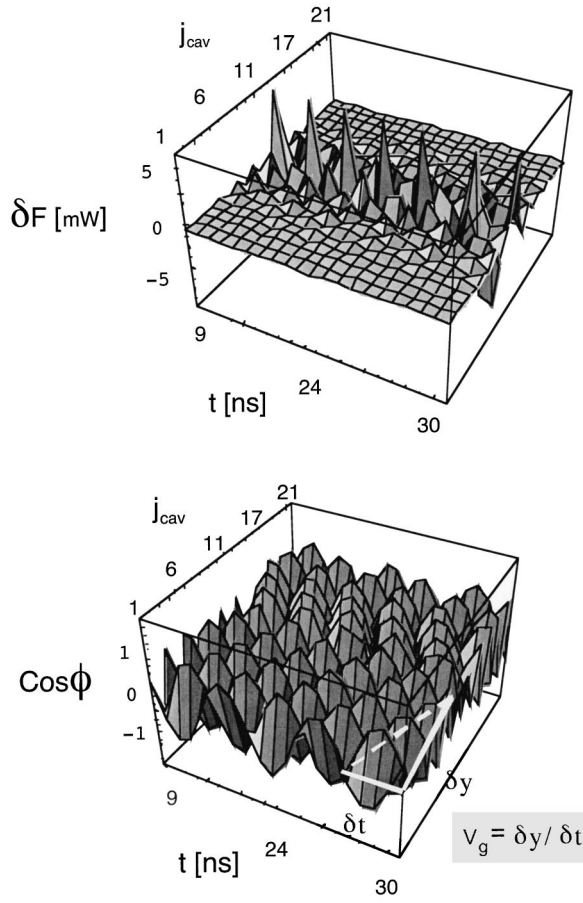


FIG. 17. Time evolution of evanescent lattice waves. Cavities maintained at constant bias, plus the central cavity $j=11$, are driven with superimposed modulated bias. (a) Power perturbation. (b) Phase cosine recorded at each cite j . The envelope over all points t_n and P_j is plotted. The amplitude perturbation decays quickly to the steady-state value over most of the array, but phase perturbations propagate throughout.

sites is not π as in the spontaneous mode locking of Fig. 7, nor is it the same among all site pairs.

The decay length for driven oscillations is of obvious interest to the performance of VCSEL array based interconnects since it invites cross talk and BER when adjacent cavities are switched on. Of particular interest is the effect on the turn-on jitter, related with the effect of cavity cross coupling on the density rise and radiation rise times. Such considerations set an upper limit on the array packing density [13] and will be investigated in future work. On the other hand strongly coupled arrays may be desirable for phased array beam steering. In that case controlling the phase difference through the applied driving frequency can offer a way of fast and effective steering without micromechanical actuators.

VII. PHASE SELECTION

The observed tendency for spontaneous antiphase locking, whereby adjacent cavities phase lock in an out-of-phase $\Delta\varphi = \pi$ configuration can be understood from a free-energy point of view. In the preceding section we saw that near the

final approach to the steady state the optical modulations are described by the linearized Eqs. (37). If one were to ignore the dissipation described by the diagonal matrix elements, the undamped modulations would be described by a Hamiltonian system

$$\frac{d}{dt} \delta F = -|D_{FN}| \delta N = -\frac{\partial H}{\partial \delta N}, \quad (56)$$

$$\frac{d}{dt} \delta N = D_{NF} \delta F = \frac{\partial H}{\partial \delta F}, \quad (57)$$

where the Hamiltonian is given by

$$H(\delta N, \delta F) = \frac{1}{2} D_{NF} \delta F^2 + \frac{1}{2} |D_{FN}| \delta N^2. \quad (58)$$

The power and density fluctuations δF , δN play a role similar to the “position” and “momentum” in a mechanical system. Performing the canonical transformation $\hat{F} = \delta F / \sqrt{|D_{FN}|}$, $\hat{N} = \delta N \sqrt{|D_{FN}|}$ and noticing that $\sqrt{D_{NF}|D_{FN}|} = \hat{\Omega}$ defined in Eq. (47) puts the above in the more transparent form

$$\hat{H}(\hat{N}, \hat{F}) = \frac{1}{2} \hat{\Omega}^2 \hat{F}^2 + \frac{1}{2} \hat{N}^2. \quad (59)$$

So, a density fluctuation \hat{N} moves in an effective potential $V(\hat{F}) = 1/2 \hat{\Omega}^2 \hat{F}^2$ with $\hat{H} = \text{const}$. The oscillations $\hat{N}(t)$, $\hat{F}(t)$ are 90° out of phase so that $H_o = 1/2 \hat{N}_{mx}^2 = 1/2 \hat{\Omega}^2 \hat{F}_{mx}^2$. If the centers of the oscillations $F_o(\Delta\varphi_o)$ were far apart, the motion from an arbitrary initial F would be an oscillation about the closest (“resonant”) value $F_o(\Delta\varphi_o)$, with orbits forming an “island” in the \hat{N} - \hat{F} phase space. Nonlinear saturation terms added to Eq. (59) limit the island width $\Delta\hat{F}$ and $\Delta\hat{N}$. For example, if $(\hat{\Omega}^2/2)\hat{F}^2$ were the first term in the expansion of a harmonic potential $\hat{\Omega}^2(\cos\hat{F}-1)$, the maximum excursions would be $\Delta\hat{F} = \pm\pi$, $\Delta\hat{N} = \pm\sqrt{2}\hat{\Omega}$. We will still assume $\Delta\hat{F} \sim \pi$ without imposing harmonic conditions on Eq. (59).

Observe now, according to Eqs. (32) and (33), that the locations of the steady-state values $F_o(\Delta\varphi)$ cluster close to each other for small coupling factors $Y < Y_s$. The relative separation between the first $F_o(\Delta\varphi=0)$ and last $F_o(\Delta\varphi=\pi)$ center is given by

$$\begin{aligned} \frac{F_o(\pi) - F_o(0)}{F_o(\pi)} &= 1 - \exp\left[\frac{\alpha/\zeta}{g_0} \left(\frac{1}{1+4\Lambda+8Y} \right. \right. \\ &\quad \left. \left. - \frac{1}{1+4\Lambda-8Y} \right) \right] \\ &\simeq 8(Y-\Lambda) \frac{\alpha/\zeta}{g_0}, \end{aligned} \quad (60)$$

thus the island width $\Delta\hat{F} \sim \pi$ exceeds the separation among possible centers $F_o(0) - F_o(\pi) \sim Y F_o(0) \ll 1$. Therefore one may choose any $F_o(\Delta\varphi_o)$ as a reference point for the total-

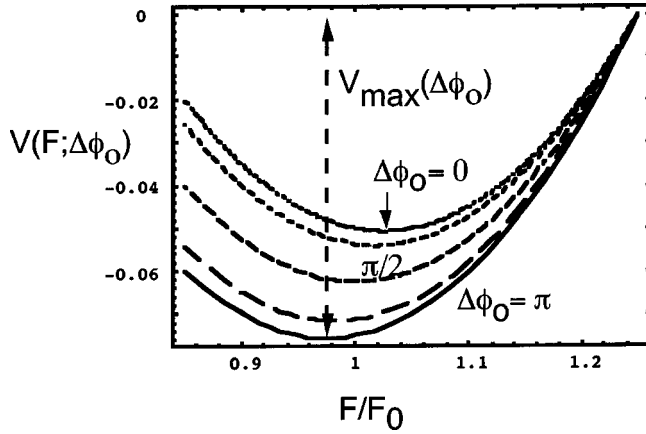


FIG. 18. Effective potentials $V(F)$ of various $\Delta\varphi$ as control parameter. The same energy value applies at the initial location $F/F_o = 1.15$. Maximum depth occurs for $\Delta\varphi = \pi$ at the bottom location $F = F_o(\Delta\varphi = \pi)$.

energy \hat{H} definition,⁸ writing the initial conditions as $\hat{F}_o = F - F_o(\Delta\varphi_o) = F_{mx}$ and $\hat{N}_o = 0$. Now, let us turn dissipation on by reviving the diagonal elements. Because $D_{NN} \gg D_{FF}$, it is the density equation which is being mostly affected,

$$\frac{d}{dt} \delta N = -D_{NN} \delta N - |D_{NF}| \delta F. \quad (61)$$

The dissipative term bears analogy to friction, proportional to the momentum in a mechanical system, furthering the analogy of \hat{N} as momentum. The motion now becomes similar to a “ball” in a potential well with friction, where the final location is the bottom of the well $\hat{F} = 0$. The potential depth depends on $\Delta\varphi_o$ as shown in Fig. 18. Since the invariants of motion are destroyed and now $H \neq \text{const}$, the fall will not stop until the deepest well bottom is reached. In other words, the final rest phase $\Delta\varphi_o$ corresponds to the maximum potential depth $F - F_o(\Delta\varphi_o)$, i.e., the lowest value for $F_o(\Delta\varphi_o)$,

$$\begin{aligned} V(\hat{F}; \Delta\varphi_o) &= \frac{1}{2} \hat{\Omega}^2 \hat{F}_{mx}^2 \\ &= \frac{1}{2} \Omega_o^2 \Xi(\Delta\varphi_o) \frac{[F - F_o(\Delta\varphi_o)]^2}{v_g \gamma_s \Xi(\Delta\varphi_o)} \\ &= \frac{\Omega_o^2}{2v_g \gamma_s} [F - F_o(\Delta\varphi_o)]^2. \end{aligned} \quad (62)$$

A crucial detail here is that the phase difference equation (31), which has not been included in Eq. (59) but nevertheless determines the value for $\Delta\varphi$, is satisfied for any $\Delta\varphi_o$ as long as the adjacent site densities and intensities are equal.

⁸The familiar from nonlinear dynamics “island overlap” situation, where $\hat{F}(t)$ can “hop” from island to island, does not apply here because only one potential term enters Eq. (59).

Use of the definitions for $F_o(\Delta\varphi_o)$, $\hat{\Omega}(\Delta\varphi_o)$, and the expansion formula $X^{1-\epsilon} = X - \epsilon \ln X$ yields

$$\begin{aligned} V(F; \Delta\varphi_o) &= \frac{\Omega_o^2}{2v_g \gamma_s} \left(F - F_o - \frac{\tilde{\gamma}}{\alpha/\zeta} N_o [4\Lambda + 4Y \cos(\Delta\varphi_o^x) \right. \\ &\quad \left. + 4Y \cos(\Delta\varphi_o^y)] \right)^2, \end{aligned} \quad (63)$$

where F_o , N_o are the uncoupled cavity steady-state values. Thus, once the system is brought near steady state, $|F - F_o(0)|/F_o(0) < 1$, the final “rest” at the deepest potential well occurs for the antiphased lock $\Delta\varphi_o = \pi$ regardless of initial F . That can also be thought of as maximizing the free energy $V(\Delta\varphi_o)$ released during the transition to a phase-locked steady state.

VIII. CONCLUSION

Coupled microlaser cavities were analyzed and shown to exhibit long-range coherence and modulation waves characterized by a lattice dispersion. For low coupling strengths (low packing density), spontaneous phase lock into a “crystal” state is numerically observed. Oscillations about this steady state are stable for modest coupling strengths. The preferred locked phase is determined by an effective “lattice potential” minimum. The generic behavior of nonlinear dissipative systems anticipates transitions from the above solutions regular in space and independent of time, to quasiperiodic and finally chaotic spatiotemporal lattice oscillations under increasing driving current J . Here we observed these transitions for increasing *coupling strength* Y under a bias constant in time and uniform in space. Therefore the lattice stability boundaries are curves in the Y - J parameter space that can be crossed in either direction. Interestingly the lattice crystallization fails for high coupling strengths (very small cavity separation), placing a stability limit on the packing density. The inclusion of longer-range interactions among further than next neighbor sites may modify those stability boundaries. Coherence may also be destroyed at very low coupling strengths due to spontaneous phase noise, but the noise floor is not analyzed here.

The present analysis suggests two methods, one static and one dynamic, of controlling the phase difference in phase-locked arrays without individual addressing. For example, one could impose the desired Bragg condition in a phase-locked array and use it for beam steering. In the static approach the minimum-energy phase for the lattice potential can be tailored by interlacing two lattices, each with different cavity properties, as in lattices with two kinds of atoms. A study of how a binary array may spontaneously settle into a selected phase will be the subject of future work. In the dynamic approach one may control the phase difference among the phase-locked neighbors by driving a collective array mode of frequency $\Omega(\kappa)$ corresponding to the desired $\kappa_{x,y} = \Delta\varphi/b_{x,y}$. In principle, that can be achieved by imposing a small oscillating current component on top of the constant bias driving the array as in Figs 17. A sub-micron time for mode locking and change in the beam direction could be

achieved. One advantage of both methods is that they do not rely on moving mechanical parts, such as mirrors.

APPENDIX A: ORTHONORMAL BASIS

Strictly speaking the original GL basis functions are not lattice orthogonal,

$$\begin{aligned} & \int_0^\infty d^2\mathbf{r} U^*(\mathbf{r}-\mathbf{R}_{ij}) U(\mathbf{r}-\mathbf{R}_{i'j'}) \\ &= \int_0^\infty d^2\mathbf{r} U^*(\mathbf{r}) U(\mathbf{r}-\mathbf{R}_{i'-i, j'-j}) \neq \delta_{i,i'} \delta_{j,j'}. \end{aligned} \quad (\text{A1})$$

An orthonormal basis $U \rightarrow \hat{U}$ is readily constructed following the Gramm-Smith orthogonalization procedure, yielding

$$\hat{U}_{(1)}(\mathbf{r}) = U_{(0)}(\mathbf{r}) - \sum_{i'=i\pm 1} \sum_{j'=j\pm 1} h_{ij}^{(1)} U(\mathbf{r}-\mathbf{R}_{ij}), \quad (\text{A2})$$

$$\hat{U}_{(n)}(\mathbf{r}) = \hat{U}_{(n-1)}(\mathbf{r}) - \sum_{i'=i\pm n} \sum_{j'=j\pm n} h_{ij}^{(n)} U(\mathbf{r}-\mathbf{R}_{ij}), \quad (\text{A3})$$

with $U_{(0)} = U$, and h_{ij} given by

$$h_{ij}^{(n)} = \int_0^\infty d^2\mathbf{r} \hat{U}_{(n-1)}^*(\mathbf{r}) U(\mathbf{r}-\mathbf{R}_{ij}). \quad (\text{A4})$$

Each iteration imposes orthogonality among further away sites. Note that h_{ij} are small (of order $Y \ll 1$) and that $h^{(n)} \sim h^{(1)^n$. For nearest-neighbor interaction only the first step is needed, whereupon $\hat{U}_{(1)}$ is divided by $\sqrt{1-8h_{11}^2}$ for normalization. Using the hatted basis \hat{U} instead of U in the coupling coefficients definitions Y , Λ , Eqs. (27) and (28) cause a second-order correction $O(Y^2)$, comparable to the second nearer site coupling strength, which is neglected in the nearest-neighbor model. The frequency is not affected by the orthogonalization, and the spatial eigenfunctions $\hat{U}_{mn}(\mathbf{r})$ correspond to the same frequency ω_{mp} as the paraxial eigenmodes $U_{mn}(\mathbf{r})$.

APPENDIX B: STABILITY EQUATIONS AROUND FIXED POINTS

Equations (24) and (25) are expanded around the steady-state values $F_{ij} = F_o$, $N_{ij} = N_o$, $\Delta\varphi_{ij} = \Delta\varphi_o$. Due to periodicity, an arbitrary (i,j) is chosen as reference; we take $i=j=0$ with near neighbors $i' = \pm 1$, $j' = \pm 1$. The perturbations are themselves Bloch waves, meaning that the next site perturbations are phase shifted by κb relative to the reference cite, $\delta A_{0,\pm 1} = \delta A_{\pm 1,0} = \delta A_o \exp(\pm i\kappa b)$, where A stands for F or N . Letting $\cos \Delta\varphi_o = [\exp(i\Delta\varphi_o) + \text{c.c.}]/2$ and taking the variation with respect to δF , δN , using the notation $D_{XY} \equiv \partial(\dot{X})/\partial Y$ with X, Y being either δN or $\delta \mathcal{E}$ yields

$$D_{NN} = -\gamma - 2BN_o - \frac{g_0 F_o}{N_o} [(1+4\Lambda) + 2(4Y \cos \Delta\varphi_o)], \quad (\text{B1})$$

$$D_{NF} = g_0 \ln \left(\frac{N_o}{N_{tr}} \right) \left[(1+4\Lambda \cos \kappa b) + \frac{1}{2} (4Y \cos \Delta\varphi_o + 4Y \cos[\Delta\varphi_o + \kappa b]) \right], \quad (\text{B2})$$

$$D_{FN} = v_g \zeta \frac{g_0 F_o}{N_o} [(1+4\Lambda \cos \kappa b) + 2(4Y \cos \Delta\varphi_o)], \quad (\text{B3})$$

$$D_{FF} = -v_g \alpha + v_g \zeta g_0 \ln \left(\frac{N_o}{N_{tr}} \right) \times \left[(1+4\Lambda) + \frac{1}{2} (4Y \cos \Delta\varphi_o + 4Y \cos[\Delta\varphi_o + \kappa b]) \right]. \quad (\text{B4})$$

When taking the partial derivatives, we used $\sqrt{F_o/F_{\pm 1}} = \sqrt{F_{\pm 1}/F_o} = \sqrt{F_o/F_o} = 1$ due to the uniformity of the steady state, and the fact that $\delta A_{\pm 1}$ introduces the additional phase shift $\pm \kappa b$. Above we used the same $\Delta\varphi_o^x = \Delta\varphi_o^y = \Delta\varphi_o = \kappa b$ and $\kappa_x = \kappa_y = \kappa$; generalizing for $K_x \neq K_y$, letting $4 \cos(\Delta\varphi_o) \rightarrow 2 \cos(K_m b) + 2 \cos(K_n b)$, $4 \cos(\Delta\varphi_o + \kappa b) \rightarrow 2 \cos(K_m b + \kappa_x b) + 2 \cos(K_n b + \kappa_y b)$ and then using the steady-state relations (32) and (33) in Eqs. (B1)–(B4) yields Eqs. (38)–(41).

It may appear that a complete analysis of the three coupled equations (24), (25), and (31) requires a simultaneous linearization of Eq. (31) subject to $\Delta\varphi \rightarrow \Delta\varphi_o + \delta\varphi$. However, in order to conform with the Bloch condition, the phase shift among adjacent sites is not an independent variable but a parameter assuming a fixed value $\delta\varphi = \kappa b$; the complex perturbation $\delta A_o \exp(\pm i\kappa b)$ used in Eqs. (24) and (25) already involved an *arbitrary large* $\delta\varphi = \kappa b$. It is also worth noting that, if one still elects to linearize Eq. (31) choosing a small $\delta\varphi \ll 1$, the phase corrections enter to the second order and the linear stability is still determined by Eqs. (B1)–(B4). Indeed we must have $\delta A_{0,\pm 1} = \delta A_{\pm 1,0} = \delta A_o \exp[\pm i\delta\varphi]$ (i.e., not $\delta A_o + A_o \exp[\pm i\delta\varphi]$), and since all amplitude terms in the phase evolution Eq. (31) are like $A_o/A_{\pm 1,0}$, the perturbation yields

$$\begin{aligned} \frac{A_o}{A_{\pm 1,0}} &\rightarrow \frac{A_o(1+\delta A)}{A_o(1+\delta A e^{\pm i\delta\varphi})} \\ &= 1 \pm i\delta A \delta\varphi + \delta A^2 \\ &= 1 + O(\delta A^2). \end{aligned} \quad (\text{B5})$$

That, and the uniform steady-state densities, yield zero partial derivatives $\partial(\dot{\Delta}\varphi)/\partial N = \partial(\dot{\Delta}\varphi)/\partial F = \partial(\dot{\Delta}\varphi)/\partial \Delta\varphi = 0$. Hence the 3×3 stability matrix reduces to a 2×2 case,

$$\det \begin{vmatrix} -D_{NN}-\lambda & D_{NF} & D_{N\Phi} \\ D_{FN} & -D_{FF}-\lambda & D_{F\Phi} \\ 0 & 0 & 0-\lambda \end{vmatrix} \\ = -\lambda \det \begin{vmatrix} -D_{NN}-\lambda & D_{NF} \\ D_{FN} & -D_{FF}-\lambda \end{vmatrix} = 0, \quad (\text{B6})$$

even though $D_{N\Phi} = \partial(\dot{N})/\partial\Delta\varphi$ and $D_{F\Phi} = \partial(\dot{F})/\partial\Delta\varphi$ are not zero. Here, the entire system stability is determined by the stability of the F, N dynamic subspace; the subspace spanned by $\Delta\varphi$ is the center manifold of marginal stability, contributing the trivial eigenvalue $\lambda=0$ in Eq. (B6).

APPENDIX C: CHAOTIC REGION

Although regular orbits are absent in the chaotic region, the stability relation is useful in the following sense. Consider an arbitrary trajectory passing through an arbitrary (nonfixed) point $F(t_o), N(t_o)$ at $t=t_o$ and a nearby orbit passing from $F(t_o)+\Delta F, N(t_o)+\Delta N$. For short time intervals $t_o+\delta t$ the time evolution of the trajectory separation $\delta F(t), \Delta N(t)$ is still given by an expression similar to Eq. (37),

$$\frac{d}{dt} \begin{pmatrix} \Delta N \\ \Delta F \end{pmatrix} = \begin{pmatrix} -\tilde{D}_{NN} & \tilde{D}_{NF} \\ \tilde{D}_{FN} & -\tilde{D}_{FF} \end{pmatrix} \begin{pmatrix} \Delta N \\ \Delta F \end{pmatrix}, \quad (\text{C1})$$

where the tilde symbol now implies that the partial derivative $\tilde{D}_{XY} \equiv \partial(\dot{X})/\partial Y$ is given by the primitive expressions for arbitrary F, N in Appendix B [i.e., not substituting the fixed-phase values in Eqs. (C1)–(C4)]. After diagonalization, the infinitesimal evolution of the orbit separation is $\Delta\mathbf{X}(t_o + \Delta t) = \Delta\mathbf{X}_o \exp(\lambda_o \Delta t)$, where $\Delta\mathbf{X}$ is the orthonormal base corresponding to λ_o . For $\lambda_o > 0$ nearby orbits diverge, $\Delta\mathbf{X}(t_o + \Delta t)/\Delta\mathbf{X}(t_o) = 1 + \lambda_o \Delta t > 1$. One can repeat the process and define the local orbit divergence $\Delta\mathbf{X}(t_n + \Delta t)/\Delta\mathbf{X}(t_n)$ at any phase-space point and time. If the matrix (C1) is positive definite $\lambda_n > 0$ for every n , meaning that the instability criterion $Y > Y_{abs}$ in Eq. (54) is satisfied for any F, N over the phase-space area considered, the Liapunov exponent $h \equiv \lim_{N \rightarrow \infty} (1/N) \ln \prod_{n=1}^N (\Delta\mathbf{X}_{n+1}/\Delta\mathbf{X}_n)$ of the system is greater than unity leading to chaotic orbits, justifying the conjecture of Sec. V. That is a sufficient but not necessary condition, since h can exceed unity without all λ_n being positive (i.e., not every $1 + \lambda_n \Delta t > 1$); in fact we observe chaotic behavior below the limit Y_{abs} .

-
- [1] K. Iga, F. Koyama, and S. Kinoshita, *IEEE J. Quantum Electron.* **24**, 1845 (1988).
- [2] J. P. van der Ziel, D. G. Deppe, N. Chang, G. J. Zyzdik, and S. N. G. Chu, *IEEE J. Quantum Electron.* **26**, 1873 (1990).
- [3] D. Zhou, L. J. Mawst, and Z. Dai, *IEEE J. Quantum Electron.* **38**, 652 (2002).
- [4] M. Grabherr, M. Miller, R. Jager, R. Michalzick, U. Martin, H. J. Unold, and K. J. Ebeling, *IEEE J. Sel. Top. Quantum Electron.* **5**, 495 (1999).
- [5] K. Butler, D. E. Ackley, and D. Botez, *Appl. Phys. Lett.* **44**, 293 (1984); **44**, 935(E) (1984).
- [6] D. Botez and A. P. Napartovich, *IEEE J. Quantum Electron.* **30**, 975 (1994); **32**, 2175(E) (1996).
- [7] J. W. Scott, B. J. Thibeault, C. J. Mahon, L. A. Coldren, and F. H. Peters, *Appl. Phys. Lett.* **65**, 1483 (1994).
- [8] J. D. Joannopoulos, R. D. Meade, and J. N. Winn, *Photonic Crystals* (Princeton University, Princeton, NJ, 1995).
- [9] O. Painter, J. Vuckovic, and A. Scherer, *J. Opt. Soc. Am. B* **16**, 275 (1999).
- [10] S. Riyopoulos, *J. Opt. Soc. Am. B* **19**, 1544 (2002).
- [11] See, for example, S. L. Chuang, *Physics of Optoelectronic Devices* (Wiley Interscience, New York, 1995), pp. 429,430.
- [12] S. Riyopoulos, D. Dialetis, J. Liu, and B. Riely, *IEEE J. Sel. Top. Quantum Electron.* **7**, 312 (2001).
- [13] S. Riyopoulos, in *Modulation Waves Propagating in VCSEL Arrays*, Proceedings of SPIE, Photonics West, 2001, edited by K. Coquette (SPIE, San Jose, CA, 2001), pp. 142–147; in *Simulation of Transient Dynamic Behavior in Laterally Coupled VCSEL Arrays*, Proceedings of SPIE, Photonics West, 2002, edited by C. Lei and S. P. Kilcoyne (SPIE, San Jose, CA, 2002), pp. 179–182.